Auditory nerve fiber excitability for alternative electrode placement in the obstructed human cochlea: electrode insertion in scala vestibuli versus scala tympani

Journal of Neural Engineering

PAPER

Auditory nerve fiber excitability for alternative electrode placement in the obstructed human cochlea: electrode insertion in scala vestibuli versus scala tympani

Andreas Fellner[1,3,*], Cornelia Wenger[1,3,*], Amirreza Heshmat[2] and Frank Rattay[1]

[1] Institute for Analysis and Scientific Computing, Vienna University of Technology, Vienna, Austria
[2] Department of Imaging Physics, University of Texas MD Anderson Cancer Center, Houston, TX, United States of America
[3] These authors contributed equally to this work.
[*] Authors to whom any correspondence should be addressed.

E-mail: andreas.fellner@tuwien.ac.at and cornelia.wenger@tuwien.ac.at

Keywords: cochlear implant, finite element model, multi-compartment model, scala vestibuli, auditory nerve fibers

OPEN ACCESS

RECEIVED
29 December 2023

REVISED
27 June 2024

ACCEPTED FOR PUBLICATION
19 July 2024

PUBLISHED
1 August 2024

Abstract

Objective. The cochlear implant (CI) belongs to the most successful neuro-prostheses. Traditionally, the stimulating electrode arrays are inserted into the scala tympani (ST), the lower cochlear cavity, which enables simple surgical access. However, often deep insertion is blocked, e.g. by ossification, and the auditory nerve fibers (ANFs) of lower frequency regions cannot be stimulated causing severe restrictions in speech understanding. As an alternative, the CI can be inserted into the scala vestibuli (SV), the other upper cochlear cavity. *Approach*. In this computational study, the excitability of 25 ANFs are compared for stimulation with ST and SV implants. We employed a 3-dimensional realistic human cochlear model with lateral wall electrodes based on a μ-CT dataset and manually traced fibers. A finite element approach in combination with a compartment model of a spiral ganglion cell was used to simulate monophasic stimulation with anodic (ANO) and cathodic (CAT) pulses of 50 μs. *Main results*. ANO thresholds are lower in ST (mean/std = μ/σ = 189/55 μA) stimulation compared to SV (μ/σ = 323/119 μA) stimulation. Contrary, CAT thresholds are higher for the ST array (μ/σ = 165/42 μA) compared to the SV array (μ/σ = 122/46 μA). The threshold amplitude depends on the specific fiber-electrode spatial relationship, such as lateral distance from the cochlear axis, the angle between electrode and target ANF, and the curvature of the peripheral process. For CAT stimulation the SV electrodes show a higher selectivity leading to less cross-stimulation of additional fibers from different cochlear areas. *Significance*. We present a first simulation study with a human cochlear model that investigates an additional CI placement into the SV and its impact on the excitation behavior. Results predict comparable outcomes to ST electrodes which confirms that SV implantation might be an alternative for patients with a highly obstructed ST.

1. Introduction

Unaddressed hearing loss impacts cognition and negatively affects communication, education, and employment which might lead to social isolation or loneliness. The World Health Organization estimates that by 2050 nearly 2.5 billion people might have some degree of hearing loss and at least 700 million will require hearing rehabilitation (World Report on Hearing 2021). A cochlear implant (CI) consists of a flexible silicone array containing electrical contacts which stimulate auditory nerve fibres (ANFs) directly in order to initiate nerve signals in people with severe to profound hearing loss. CIs belong to the most successful neuro-prosthetic devices with already one million estimated users globally (Zeng 2022).

1.1. Clinical issues, performance after implantation in scala tympani vs. scala vestibuli

The scala tympani (ST) which is the lower cochlear duct (figure 1) is considered as an initial and approachable way for CI array insertion. Partial or total cochlear obstruction occurs when the ST shows

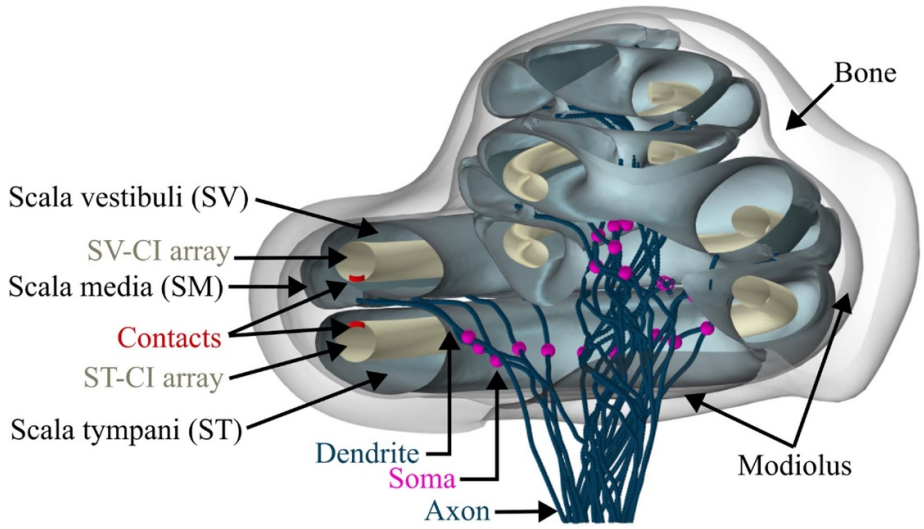

Figure 1. Human cochlear model with two electrodes (red plates) and nerve fiber pathways. 95% of the auditory nerves are afferent bipolar spiral ganglion cells consisting of dendrite (peripheral process), soma (magenta) and axon (central process). In this scheme, the upper electrode represents a scala vestibuli implant, the lower one a scala tympani CI.

impediments that might be present due to ossification, fracture, tumor of the temporal bone, otosclerosis, post-meningitis fibrosis, chronic otitis media, or autoimmune inner ear diseases (Green *et al* 1991, Balkany *et al* 1996, Kiefer *et al* 2000, Bacciu *et al* 2002, Rinia *et al* 2006, Coelho and Roland 2012). Clinical studies reported that up to 15% of all CI candidates suffer from cochlear obstruction, and this probability is even raised to 80% for CI candidates who become deaf because of meningitis (Rinia *et al* 2006). Therefore, adapted methods are used to provide insertion into the blocked ST, such as removing or drilling ossification and making a tunnel through the basal turn of the cochlea for a full or partial electrode array insertion (Balkany *et al* 1996, Rinia *et al* 2006).

In case of a non-obstructed ST, clinical studies reported good speech perception for full CI array insertion (Geier and Norton 1992, Kiefer *et al* 2000, Yukawa *et al* 2004, O'Connell *et al* 2017). However, when the degree of ST obstruction increases, the benefits of the high number of active electrodes for full CI insertion drastically diminish (Rinia *et al* 2006). Reducing the active electrode number is done by postoperatively turning off electrodes that may eventually cause device failure (Zeitler *et al* 2009). Moreover, deep insertion often causes damage to sensitive cochlear structures, which can be mitigated by using highly flexible CIs. As discussed by Hochmair *et al* (2015) such CIs have their benefits including faithful sound coding and reduced surgical traumaticity. For example, the MED-EL Soft series consists of a wide range of free-fitting lateral wall electrodes offering long active stimulation ranges with full cochlear coverage. Thus, the theoretical investigation presented in this study will analyze insertion depths of up to 700°.

Scala vestibuli (SV) implantation is a valuable alternative if ST shows impediments (Kerr and Backous 2005). Steenerson *et al* (1990) inserted a CI array in the SV of two patients who suffered from post-meningitis ST obstruction by ossification and fibrosis. The results predicted comparable outcomes as expected for a ST CI. Pijl and Noel (1992) studied SV implantation in one patient who initially received a CI array in ST that, after a while, was removed due to subsequent infections in the ST and then inserted in the SV. They reported equivalent results between former ST and later SV implantation. A recent study confirmed full SV insertion and predicted electrical stimulation of neuronal elements across all frequencies (Holzmeister *et al* 2022). Furthermore, some studies even published a slightly better performance of SV CIs (Balkany *et al* 1996, Kiefer *et al* 2000, Bacciu *et al* 2002, Leonor and Santiago Luis 2004, Lee *et al* 2019). Trudel *et al* (2018) published that not only the outcome was equivalent between ST and SV CI users, but also, interestingly, the sentence recognition in a noisy environment was better in patients who received a CI in SV. Additionally, the SV implant user in the bilateral CI case also had better speech discrimination in noise (Leonor and Santiago Luis 2004). However, according to other studies word recognition scores with electrodes in SV were significantly lower than in ST (Finley *et al* 2008, Holden *et al* 2013, O'Connell *et al* 2016, Shaul *et al* 2018). This discrepancy may be based on differences in the damage of sensible structures such as the organ of Corti or Reissner's membrane.

Clarifying the serious disagreement in auditory outcomes for CIs at SV versus ST is hindered as (i) all relevant clinical results are based on small numbers of comparable recipients, (ii) supposable large differences exist in their neural ANF status

and (iii) individual cognitive ability to decode the artificially generated neural patterns varies among patients. However, computational modeling is an excellent alternative tool to analyze the artificially generated pattern in ANFs under comparable conditions. Here, we compare the auditory nerve excitability for CI in SV versus ST assuming healthy ANF status, monophasic stimulation and lateral electrode placement.

1.2. Modeling studies of electrically stimulated ANFs

The key element for the electrical excitation of ANFs is the non-linear conductance of voltage sensitive ion channels in the active cell membrane, which is found at the peripheral terminal, the nodes of Ranvier and in the soma region. In comparison with other membrane models, a model with Hodgkin-Huxley dynamics (Hodgkin and Huxley 1952, Rattay and Aberham 1993, Rattay *et al* 2001b) seems to mimic several properties seen in human ANF experiments quite well (Bachmaier *et al* 2019). This surprising observation was further confirmed by a double pulse experiment with CI users (Motz and Rattay 1986).

In early studies of the electrically stimulated auditory nerve neuron, also called a spiral ganglion neuron, 1-dimensinal (1D) approaches have been employed to find the best fit for geometric model parameters. For example Colombo and Parkins (1987) found 10 μm to be the best fit for the length of the non-myelinated terminal for matching results with measured chronaxie values. The authors also employed their model to study the barrier of the soma, yet assuming a myelinated soma and perfectly insulated internodes. However, in contrast to other mammals the soma of a human spiral ganglion neuron is without myelin or only covered by a single satellite glia cell (Nadol 1988, Rattay *et al* 2013). Consequently, the high capacitance of the human soma is a barrier in spike conduction that demands for a strong intracellular current flow which is generated by the active membrane of a rather long (100 μm) non-myelinated pre-somatic segment (Rattay *et al* 2001b).

In order to study extracellular stimulation at least a 2-dimensional (2D) pathway of the ANF needs to be considered. The trans-membrane voltage of compartment n is described mathematically by an ordinary differential equation where the stimulating driving force depends on the external voltage differences between neighboring compartments. Consequently, in a region where several compartments have the same extracellular potential V_e these differences cancel out which deems this region to be insensitive to extracellular stimulation. This emphasizes the importance of convincing V_e values along the pathways of the ANFs for accurate analysis of their excitation.

Thus, for a good simulation we need (i) an accurately calculated electric field as established by the CI electrode, (ii) plausible pathways of the ANFs, and (iii) a satisfying compartment model implementing the dynamics of the cell membrane. Typically, the extracellular potentials induced inside the human cochlea are inferred from the calculated field (i) using the finite element method (Hanekom and Hanekom 2016) or the boundary element method (Kalkman *et al* 2014, 2015). The geometry data (ii) can be found from μ-CT scans (Bai *et al* 2019) or from a mid-modiolar cross-sectional image (Rattay *et al* 2001a, Nogueira *et al* 2016).

In the presented computational study, we employed a 3-dimensional (3D) human cochlear model reconstructed from μ-CT scans (Potrusil *et al* 2020) to analyze the excitability of 30 realistic ANFs that have been manually traced from base to apex of the cochlear (Potrusil *et al* 2020). Threshold profiles were investigated for equivalent CI electrode arrays placed in the ST and SV. Considering common CI array dimensions (Zeng *et al* 2008, Dhanasingh and Jolly 2017) it was possible to study a total of 25 target electrodes in each scala that are in direct vicinity to one of the ANFs. The initiation and propagation of nerve signals were recorded for monophasic pulses of both polarities.

2. Methods

Our computational pipeline for studying the excitation profiles of ANFs is presented in the following sections. In short, a finite element model (FEM) of the human cochlea (Potrusil *et al* 2020) together with a CI array implemented in COMSOL Multiphysics 6.1 (www.comsol.com) was used to compute the extracellular potential along realistic ANFs. Then the spiking behavior of the ANFs was simulated in NEURON 8.2 (Carnevale and Hines 2006) with a well-established compartment model of cochlear neurons (Rattay *et al* 2001b, Heshmat *et al* 2021) where the calculated extracellular potential distributions from the FEM served as an input. The whole pipeline was controlled by a custom-written python script that ran on a server with 64 parallel threads with 256 GB RAM. To control and access the COMSOL model, the python library MPh 1.2.3 (https://github.com/MPh-py/MPh) was used in combination with COMSOL batch commands. The NEURON model was fully implemented and controlled by using NEURON's python interface.

2.1. Cochlear geometry and ANF pathways

For the generation of the 3D cochlear model we adapted a previous segmentation of a μ-CT dataset of a human cochlea (Potrusil *et al* 2020). The model consists of 5 different electrical domains, namely SV and ST, scala media (SM), modiolus (including the osseous spiral lamina) and surrounding bone

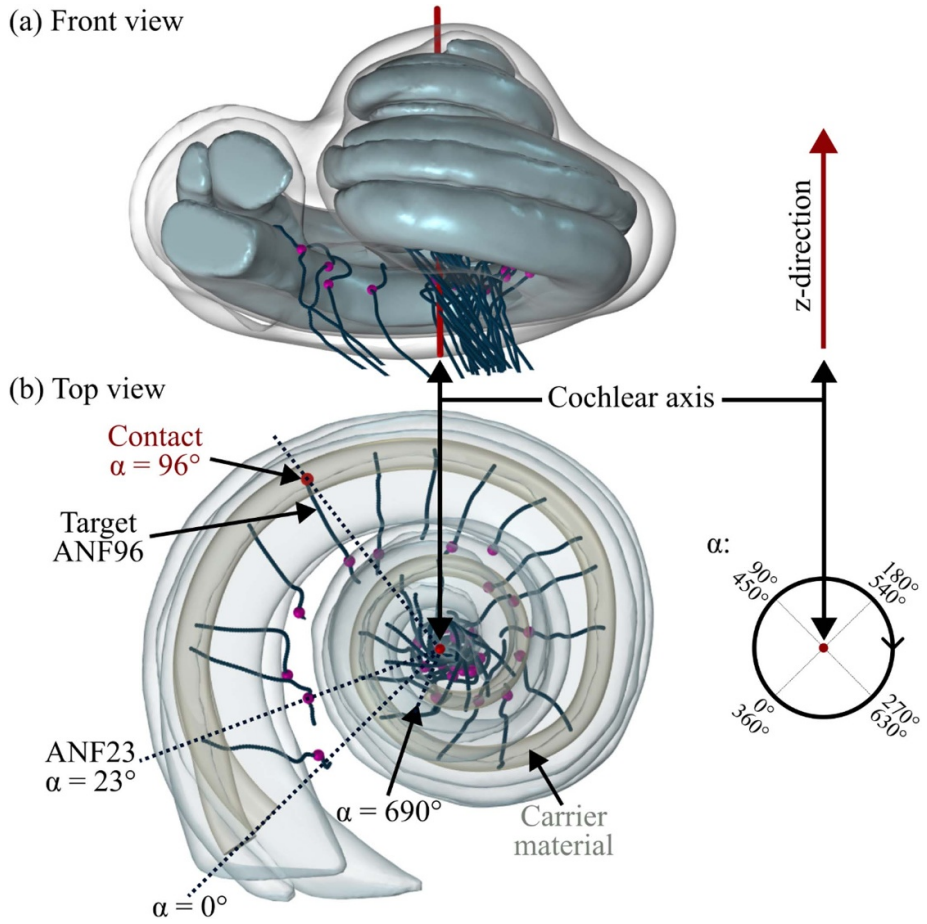

Figure 2. Front view and top view of the used cochlear model. The front view (a) shows the ducts embedded in the modiolus and bone. The ANFs originating between the ST and SV spiral down in the center of the cochlea close to the cochlear axis (z-direction). The angle α defines the angular position around the cochlear axis. The top view (b) shows the two electrode arrays starting at $\alpha = 0°$ and ending at $\alpha = 690°$ without any violation of the outer boundaries of the respective duct. Both arrays are perfectly aligned except for the very beginning of the silicone carrier ($\alpha < 18°$). ANF auditory nerve fiber, ST scala tympani, SV scala vestibuli, SM scala media.

(figures 1 and 2). Some adaptions and improvements have been made utilizing MeshLab software (Cignoni *et al* 2008) to ensure a continuous Reissner's membrane between SV and SM, and the absence of holes or intersections between different domains. This process resulted in watertight, high quality meshes in STL-format without any non-manifold edges or vertices.

Based on this geometry, a cochlear axis (z-direction) was defined and acts as a reference for further geometric operations. The azimuthal angel α defines the angular position around the cochlear axis and is used to define positions along the spiral shaped ducts (figure 2).

Similarly, the ANF pathways were based on a previously traced dataset of another specimen (Potrusil *et al* 2012, 2020). Only the affine image registration was available which does not account for the non-linear morphing between two individual cochleae of specific shape and size. As a result, some of the originally traced points intersect with the cochlear ducts which prevents anatomically realistic pathways where ANFs run exclusively through the modiolus domain which includes the osseous spiral lamina. To ensure correct association of electrical conductivities which affect the stimulation-induced extracellular potential distribution along the ANFs, we slightly modified the original data mainly in terms of minimal spatial translation of the ANFs preserving original pathways and interesting detail such as the fanning out of the dendrites and the mid-modiolar spiraling pattern of axons.

After preliminary smoothing of the 30 traced pathways 16 ANFs were lying too far away from the cochlear axis resulting in intersections with the ST at the mid-modiolar region and extra-long dendrites at the lateral end. Thus, for each fiber a specific translation vector has been applied which kept the ANF angle similar to the original data. In a subsequent step, we corrected for vertical discrepancies of some ANFs which were too high and thus crossing the SV. Simultaneously, we reduced the bias of a more favorable electrode placement in either scala by applying a vertical shift parallel to the cochlear axis to all but one fiber. The specific translation vector was found by calculating the median thickness of the osseous spiral lamina (figure 4) evaluated along

an appropriate section of the peripheral process. The combined total translation vector of these two steps had a median length of 143 μm among all 30 ANFs.

Lastly, we guaranteed a uniform start of all dendrites that reached 50 μm into the SM where the synaptic connections with inner hair cells are assumed. This resulted in slightly altered peripheral process lengths compared to previous data (Potrusil *et al* 2012, 2020) with a median absolute difference of 95 μm which is less than the length of a peripheral internode. Each final ANF consisted of a spline with 2000 points, where the first point defined its angle relative to the cochlear axis (figure 2).

2.2. CI electrode arrays geometry

Two CI arrays each consisting of a silicone carrier and electrical contacts which can be individually placed along the carrier were modeled for insertion into the ST and the SV. The silicone carriers were created with a diameter tapered from 0.6 to 0.3 mm consistent with typical ranges for CI arrays (Zeng *et al* 2008, Dhanasingh and Jolly 2017). In terms of placement these CI arrays are comparable to commonly used lateral wall electrodes.

For the geometric construction, the following considerations were taken into account: (i) the arrays shall have a more or less constant distance to the first part of each ANF (at process length 100–200 μm); (ii) the arrays shall be placed as lateral as possible; and (iii), both CIs shall have the same lateral alignment in relation to the cochlear axis.

To meet these requirements, a spiraled centerline was extracted from the final 3D structure of the ST duct. This centerline was adjusted in z-direction in a way that the outer boundary of the carrier is approximately 250 ± 10 μm away from the ANFs (i). Further, the centerline was manually fitted in the lateral direction as close to the outer scala wall as possible (ii). The corresponding SV centerline was then created by accordingly translating the fitted ST centerline in z-direction by twice the ST electrode—target ANF distance (iii). A sweep operation in COMSOL was used to create the silicone carrier volumes based on the centerlines. The axial and lateral adjustments were repeated until both arrays fitted into the respective duct without violating the outer boundaries. As a result perfectly aligned arrays were created with only a small deviation in the very first beginning of the silicone carrier due to the diverging ST and SV ducts (figure 2).

Both CI arrays start at the same azimuthal angle $\alpha = 0°$ and twist for almost 2 turns until $\alpha = 690°$ (figure 2(b)). This leads to an insertion length of approximately 25 mm for both arrays, ST and SV, which translated to 25 target ANFs that could be reached directly ($23° < \alpha < 680°$). Thus, for each of the 25 target fibers a corresponding contact was created whereas the exact positions (angles α) of the contacts were evaluated individually for ST and SV arrays by minimizing the Euclidean distance between contact and its target ANF. A contact was represented as a cylindrical plate with a diameter of 0.2 mm and a height of 0.15 mm embedded in the silicone carrier. In terms of contact placement around the carrier, each active contact in the ST array is facing 'upwards' (in z-direction) directly to its target ANF, and 'downwards' for the contacts of the SV array (red 'Contacts' in figures 1 and 3).

2.3. COMSOL model setup

To create a mesh for FEM simulations the imported cochlear domain STL's were combined with geometric parts that modelled the CI arrays as described above. Additionally, a sphere of 100 mm radius has been created that encloses the whole cochlea.

The tetrahedral mesh was created individually for all domains. To preserve the round structures of the cochlear ducts, the modiolus and surrounding bone structure, and the electrodes, these domains were meshed with a maximum element size of 0.15 mm. For the outer sphere a coarse mesh was chosen. This meshing strategy provides high accuracy in the areas of interest with appropriate computational costs resulting in a total of approximately 1580 000 tetrahedral elements and approximately 4200 000 degrees of freedom due to second order element discretization (quadratic).

Electrical conductivities in S/m of all materials were assigned according to (Rattay *et al* 2001a, Potrusil *et al* 2020): 1.43 (perilymph ST and SV), 1.67 (endolymph SM), 0.0334 (modiolus), 0.016 (compact bone of the cochlear outer surface and the surrounding area), 1000 (electrodes), and 0 (silicone).

We used the Electric Currents physics of the AC/DC module in COMSOL Multiphysics to calculate the extracellular potential (V_e) distribution of the active electrode within the cochlea (figure 3). The physics setup assumed continuity on internal boundaries and a fixed current of 1 μA via the terminal boundary condition for active electrode contacts. The ground was set to the outer boundaries of the surrounding sphere to simulate the return electrode (Fellner *et al* 2022). When calculating the potential distribution of either the ST or SV electrode, the electrical properties of the respective other electrode are set to match the electrical properties of the perilymph. This way, the other electrode is not altering the electric field established by the active one (figure 3, ST vs. SV stimulation).

2.4. Compartment and neuron model setup

ANF excitation was computed with the previously described and well-established compartment model of a human type I spiral ganglion cell SGN (Rattay *et al* 2001b, Potrusil *et al* 2020). These afferent neurons have a peripheral and a central process that consist of an alternating sequence of nodes of Ranvier and

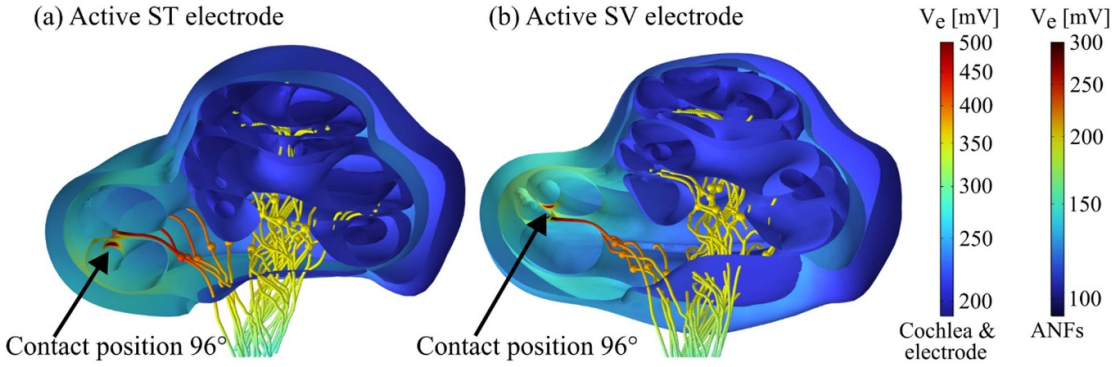

Figure 3. Electric potential distribution inside the cochlea simulated with COMSOL for ST (a) and SV (b) stimulation of target fiber ANF96. While the target fiber shows the highest gradient in the extracellular potential, also the other fibers experience changes in the V_e which might result in APs if the stimulation amplitude is high enough. Different color scales for a 150 μA pulse are applied for the cochlea and the ANF pathways. ST scala tympani, SV scala vestibuli, ANF auditory nerve fiber, V_e extracellular potential.

internodes, which are connected via a pre- and post-somatic area to a spherical soma (Rattay *et al* 2001b). The intracellular resistivity was 0.1 kΩ cm, the membrane capacitance was 1 μF cm^{-2} and the conductance of the internode was 0.1 mS cm^{-2} for each sheet of membrane (n). The dendrite is assumed to have $n = 40$ layers and the axon $n = 80$ (Arnesen and Osen 1978, Arbuthnott *et al* 1980, Spoendlin and Schrott 1989, Rattay 1990, Rattay *et al* 2002).

The ion channel kinetics were modelled according to Hodgkin Huxley (Hodgkin and Huxley 1952, Motz and Rattay 1986) with a temperature adjustment to 29 °C that fits the action potential (AP) duration in the cochlea (Rattay *et al* 2013). The soma was further surrounded by three membrane layers ($n = 3$) (Schnabl *et al* 2012). In all other active compartments, i.e. the nodes of Ranvier and the pre- and post-somatic regions and the peripheral terminal, a 10-fold increase of Hodgkin Huxley membrane conductance was accounted for experimentally reported high ion channel density (Rattay and Aberham 1993, Rattay *et al* 2002, Hossain *et al* 2005).

This physical model was implemented in NEURON with the spatial coordinates of the traced ANFs and the corresponding V_e distribution evaluated in COMSOL set through a transfer resistance via the NEURON xtra mechanism. The diameters of dendrite, axon and spherical soma were 1.3, 2.6 and 20 μm, respectively. The length of the active pre- and post-somatic regions are 100 and 5 μm, and the peripheral terminal compartment is 10 μm long. The length of a node of Ranvier is 2.5 μm, whereas peripheral and central internodes have a standard length of 125 and 500 μm. All these geometric neuron parameters were taken from Potrusil *et al* (2020) with exception of the dendritic internodal length which was halved after preliminary simulation runs showed a large CAT threshold sensitivity of node positions along the dendrite. The measured length of traced peripheral and central processes was used to determine the presence of 10–22 peripheral nodes and 13–20 central nodes.

Monophasic pulses of both polarities with a duration of 50 μs (CAT cathodic; ANO anodic pulse) were tested to investigate the excitation profile of selected neurons. A binary search algorithm was implemented to detect the threshold (stimulation amplitudes limit 1–1000 μA, resolution 1 μA), which stops at the lowest stimulation amplitude if an AP was detected by a membrane voltage over 0 mV in the second last central node. Corresponding initiation sites were defined as the first active node crossing 0 mV after the stimulus has ended.

3. Results

3.1. ANF and CI arrays' spatial relationship

The tracing data of 30 ANFs were available for this study. For investigating ANF excitation the peripheral part of the dendrite is of specific interest due to its vicinity to the lateral stimulating electrodes (figure 2). In the healthy human cochlea, each ANF starts in the SM, that contains the organ of Corti where the fiber innervates the inner hair cell, before it travels between ST and SV inside the modiolus domain towards the cochlear axis. For this study each scanned ANF was placed approximately in the middle of the modiolus domain (compare section 2.1) in order to avoid potential bias for a fiber to favor stimulation by either the lower ST or the upper SV.

The median modiolus domain thickness calculated between the first 300–500 μm in each of the 30 ANFs is presented in figure 4(a). The ANFs are displayed according to their angle respective to the cochlear axis (specific values in the legend and on top). Note that they are not uniformly aligned along the cochlea, where the minimum distance between 2 neighboring ANFs is 5° (ANF45 and ANF50) and the biggest distance is 95° (ANF830 and ANF925). The median thickness values in figure 4(a) range between

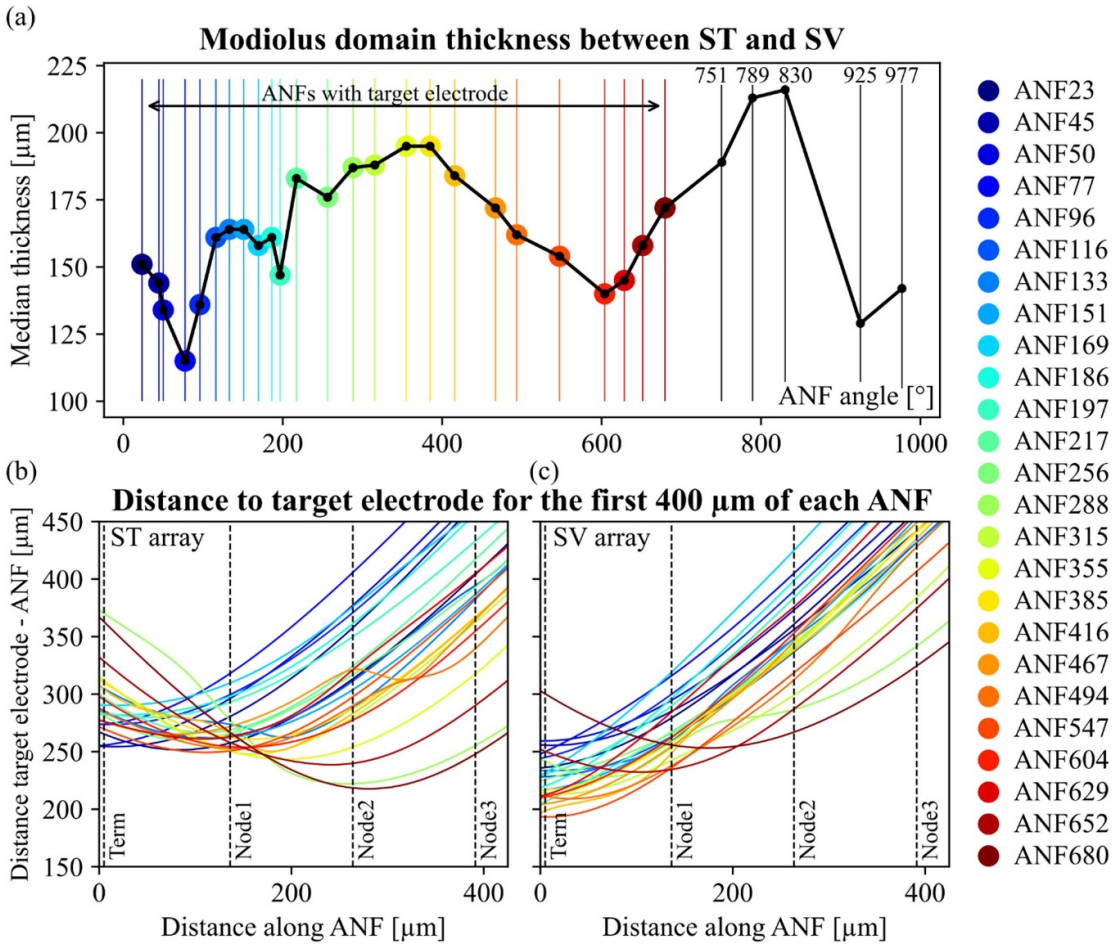

Figure 4. (a) Median thickness of the osseous spiral lamina (which belongs to the modiolus domain) calculated along the ANFs in their segments 300–500 μm from the peripheral terminal. The angle of each ANF is indicated either by their color (for 25 ANFs with a target electrode) or written at the top for the five most apical ANFs. (b) The distance to the target electrode for the first 400 μm of each ANF. Vertical dotted lines mark the terminal center (Term) and the first three nodes of Ranvier (Node1-Node3). ANF auditory nerve fiber.

115 (for ANF77) and 216 (for ANF830) μm, their median is 162 μm.

For each of the first 25 ANFs (ANF23–ANF680) we have placed two specific target electrodes, one at the ST and one at the SV array, resulting in a total of 50 active contacts which have been investigated. The distance to every individual target electrode is shown for the first 400 μm of each ANF in figure 4(b). The dotted lines indicate the center of the first 4 active compartments. Note that although the distances to each target electrode are similar at the first node when comparing ST (left) to SV (right) curves, the values at the peripheral terminal are higher for the ST. This behavior is a result of the upwards bend of the ANF into the SM for innervation, where the fiber bends towards the SV and away from the ST. The minimum electrode-ANF distance ranges from 218 (for ANF680) to 290 (for ANF169) μm with a median of 260 μm for ST and from 193 (for ANF547) to 259 (for ANF50) μm with a median of 224 μm for the SV. Also note that whereas only ANF45-ANF96 have minimal distance to the ST electrode at their first peripheral terminal, for the SV array the minimal electrode-ANF distance is almost always found at the first region with the only noteworthy exceptions of for ANF288, ANF652 and ANF680.

The centers of the active contact in both arrays have been chosen as close as possible to its target ANF. Due to the curvature of the ANFs, this resulted in slight variations of the angle of the target ANF in comparison to the calculated angle of the active contact center (figure 5(a)). For the first half of the ANFs the difference is minimal and usually below 2°, i.e. the angle of the electrode contact center is slightly lower than the angle of its target ANF (positive values above the black zero line) or slightly higher (negative values below). The highest angle difference is recorded for the last ANF680, i.e. the ST and the SV electrodes have an angle of about 670°. Differences between electrode angles of equivalent ST and SV electrodes are also mostly below 2° and only for ANF467, ANF547 and ANF494 around 4°.

The lateral distance of each target ANF was calculated as distance from the first point to the cochlear axis (figure 2). The same evaluation has been repeated for the active contact centers. The difference in the

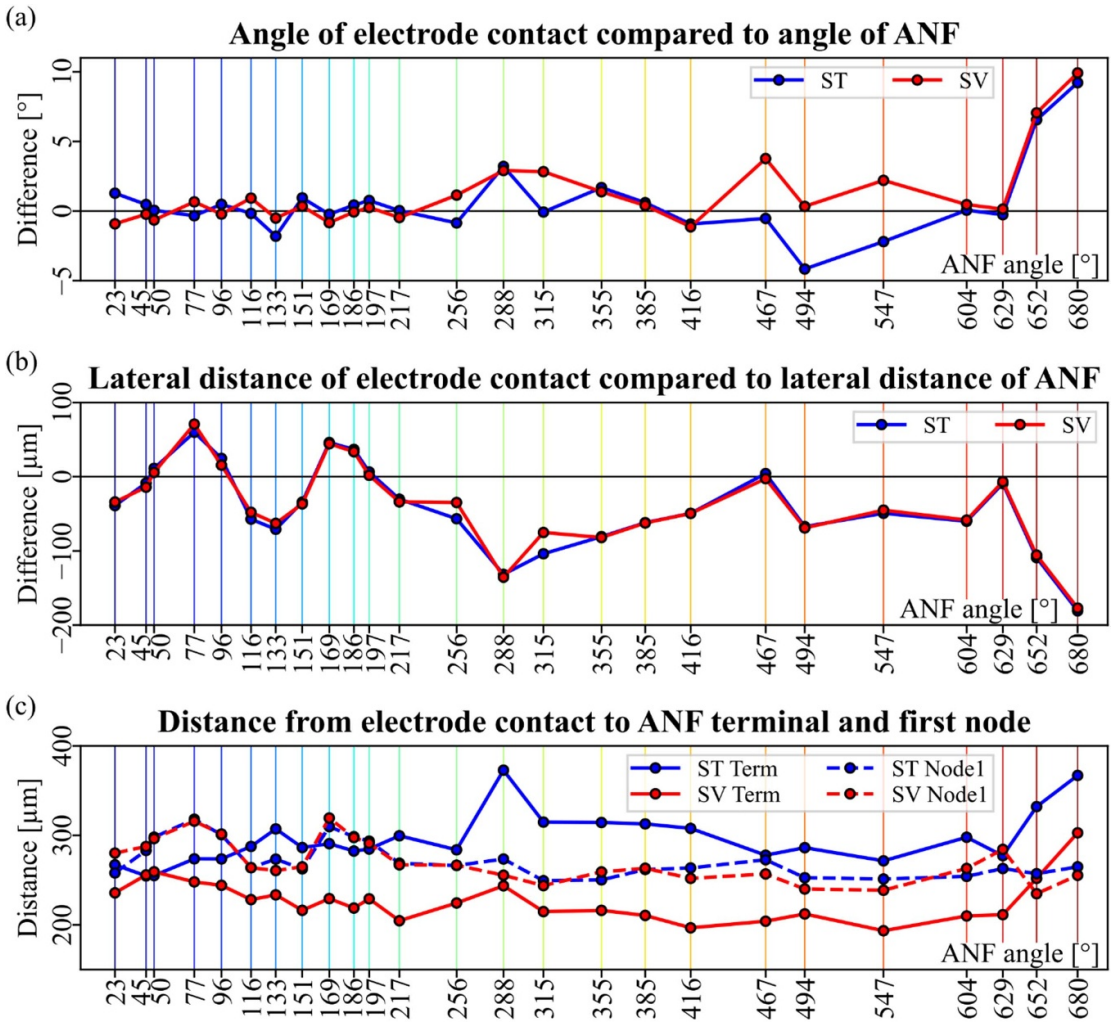

Figure 5. Electrode-target ANF spatial relationships presented for the ST (blue) and SV (red) array. (a) Angle difference between electrode center and ANF. (b) Difference in lateral distance of the electrode center and ANF. (c) Distance from electrode to terminal of ANF as solid lines and distance from electrode to the first peripheral node as dashed lines. ST scala tympani, SV scala vestibuli, ANF auditory nerve fiber.

lateral distance of electrode and target ANF is presented in figure 5(b). Positive values above the solid black line indicate that the electrode is placed more laterally, negative values represent most cases where the ANF start is more lateral. More specifically, for ST array 7 out of 25 contact positions are more lateral compared to the ANF with a lower median value of 25 μm representing the median difference in lateral distance of electrode center compared to ANF start. For the other 18 electrodes where the target ANF is more lateral this median value is -59 μm. For the SV array the situation is similar with 6 more lateral contacts and a median difference of 25 μm compared to the median difference of -50 μm for the other 19. There are indeed only slight variations in the values for ST electrodes and SV electrodes with the biggest difference between ST and SV electrodes lateral placement of 29 μm for ANF315.

The electrode-ANF distance to its terminal (solid lines) and the electrode-ANF distance to its first node (dashed lines) are reproduced in figure 5(c) for a direct comparison between ST and SV arrays and individual ANFs. As previously noted (figure 4(b)), only small variations were registered for the electrode-node1 distance in individual ANFs for ST versus SV position. This is a result of the careful and considerate contact placement for individual target fibers at equivalent positions along the CI carriers of ST and SV as explained in detail in section 2.2. About half of the ANFs are slightly closer to the ST electrode at their first node and the other half has a first node closer to the SV position. The respective difference between equivalent ST and SV electrodes for an individual ANF is only 8 μm on average with a maximum difference of 22 μm in ANF652. The minimum ANF-node1 distance for ST electrodes is 249 μm (ANF315), the maximum of 318 μm (ANF77). For SV electrodes the minimum ANF-node1 distance is 235 μm (ANF652), the maximum of 320 μm (ANF169).

In contrast to the node1 distances, for the distances from the electrode to the terminal the

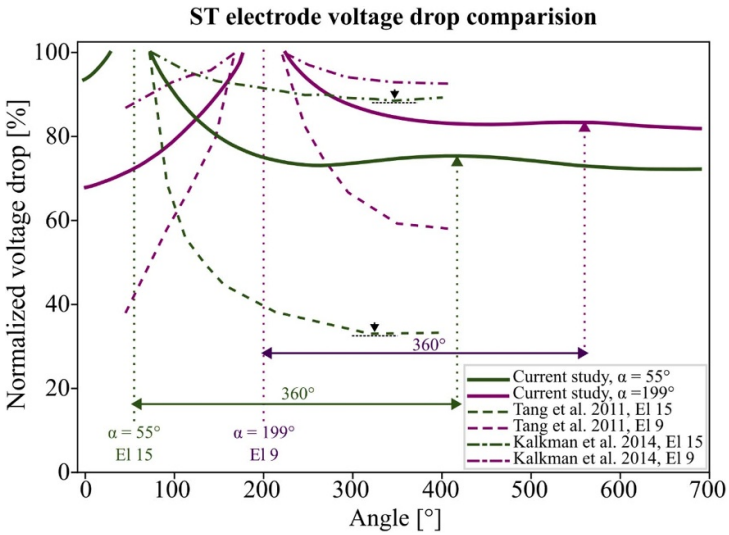

Figure 6. Comparison of the simulated intrascalar potential with published clinical data using the 16 channel HiFocus implant. The published voltage drop along the ST implant is redrawn for the stimulation with electrode 15 (dark green dashed lines) and electrode 9 (purple dashed lines). The intrascalar potential was measured at all electrodes with exception of the stimulating electrode. The corresponding voltage curves are normalized by their largest recorded values. These dashed lines are comparable with our FEM data for active electrode contacts placed at 55° (dark green) and 199° (purple) along the ST carrier. The longer extension of the simulated implant creates an additional local maximum one turn above the stimulating electrode corresponding to the +360° position marked by vertical arrows of corresponding colors. Such an expected upward trend is already seen in the patient data at least for electrode 15 (black arrowhead). ST scala tympani.

ST values are higher, i.e. a minimal distance of 255 μm for ANF45, a maximum distance of 373 μm for ANF288 and a median electrode-terminal distance for ST of 286 μm. These values for the SV array are lower with a minimum ANF-terminal distance of 193 μm for ANF547, a maximum of 302 μm for ANF680, and a median value of 224 μm. Consequently, only two fibers (ANF45, ANF50) have a terminal that is slightly closer to the ST electrode compared to the SV electrode. For all other ANFs the distance from its terminal to the target electrode is lower for the SV positions with a median difference of 75 μm and a notable maximum difference in electrode-terminal distances between ST and SV of 129 μm for ANF288. Note that the distal end of the dendrite has an upward bending to the synaptic contact with the inner hair cell which explains a reduced electrode—terminal distance of SV in comparison to ST.

3.2. Model validation

CI devices have extra equipment for measuring the decay of the intracochlear potential at each electrode contact within the array. To validate our model, we compared the simulated voltage drop in the ST implant with corresponding reported data from two clinical studies (Tang *et al* 2011, Kalkman *et al* 2014). Because of artefacts the clinical data were not measured at the stimulating electrode but at all other 15 electrodes of the used HiFocus implant and all the decays were normalized by 100% for the electrode closest to the stimulating electrode (figure 6). In order to allow for a direct comparison, we evaluated the potential along the ST carrier for additional electrode contacts placed at 55° and 199° which resulted in equivalent positions to electrode 15 and electrode 9 respectively. Our model demonstrates the typical shape of the recorded voltage decay which lies between the published ones. However, because of our larger insertion depth, an additional local maximum is clearly visible in the next turn just above both stimulating electrodes at +360° (vertical arrows of corresponding color in figure 6). This increase of the potential is already seen by stimulation with HiFocus electrode 15 at the right ending of each of the dashed dark green lines which represents the potential recorded at the most apical electrode 1.

3.3. Thresholds for anodic (ANO) and cathodic (CAT) stimulation

The threshold amplitudes for each target ANF and ST or SV stimulation with monophasic 50 μs pulses of both polarities are presented in figure 7(a). The ST values are depicted in blue, the SV values in red, CAT stimulation is presented as solid lines and ANO stimulation as dotted lines.

The presented results indicate that the lowest thresholds for AP initiation were found for CAT stimulation and SV electrodes with a median threshold of 111 μA. The lowest threshold of 92 μA was registered for ANF416, the maximum of 318 μA for ANF680 was considered an outlier. For ST stimulation the median threshold for CAT stimulation was raised to 155 μA (figure 7(b)). The lowest threshold of 93 μA was registered for ANF288, the maximum of 250 μA for ANF77.

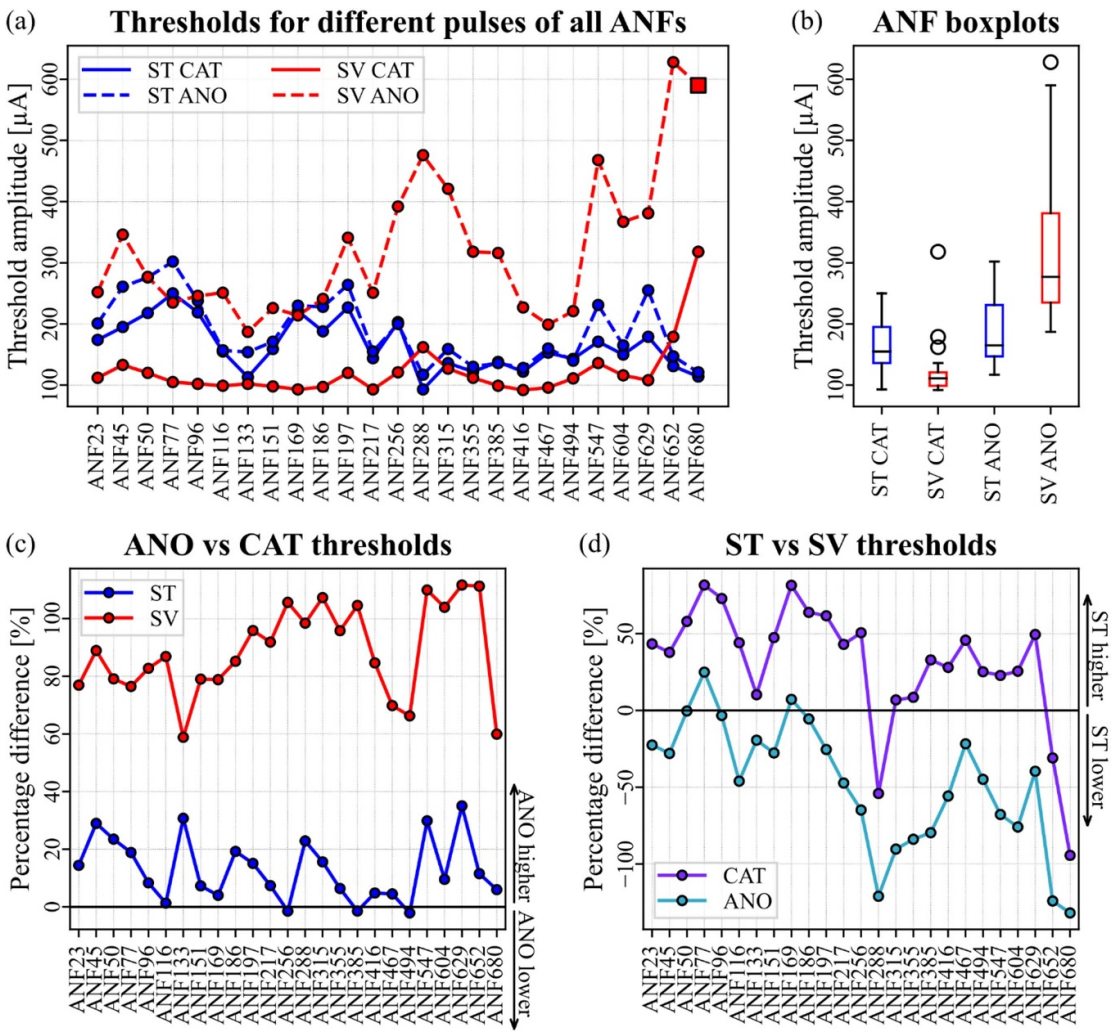

Figure 7. Thresholds for monophasic stimulation. (a) Threshold amplitudes for each ANF and both target electrodes. (b) corresponding boxplots of thresholds for all ANFs. (c) Comparison between pulse polarities. Positive percentage difference values (|A-B|/(A + B)/2) indicate lower CAT values and a negative percentage difference predicts lower ANO values. (d) Comparison between scala placement. Positive percentage difference values indicate lower SV values, and a negative percentage difference predicts lower ST values. ST scala tympani, SV scala vestibuli, ANF auditory nerve fiber, ANO anodic, CAT cathodic.

Considering ANO stimulation, the median ST threshold was 165 μA, with a minimum threshold of 117 μA for ANF288, and a maximum of 302 μA for ANF77. The highest thresholds were found for SV electrodes and ANO pulses with a median threshold of 277 μA. The lowest threshold of 187 μA was registered for ANF133, the maximum of 628 μA for ANF652.

Consequently, ANO thresholds were always much higher than the CAT values in the SV array (figure 7(c)) with a median percentage difference of 87%, whereas the lowest difference occurred for ANF133 and ANF680 and the highest for ANF652 and ANF629. For the ST array the threshold was less sensitive to a polarity switch of the stimulus current, i.e. the median percentage difference was 10% which again usually presents with lower CAT thresholds, although in ANF494, ANF256, and ANF385 the ANO thresholds were even slightly lower.

The direct comparison of ST and SV thresholds (figure 7(d)) predicts usually lower SV thresholds for CAT pulses with a median percentage difference of 43%. Yet there were exceptions, i.e. for ANF680 the SV threshold for CAT stimulation was about three times higher than the ST value, doubled for ANF288 and still higher than the ST threshold for ANF652. For ANO stimulation the ST electrodes were usually favorable with the exceptions of ANF169 and ANF77 and a median percentage difference of −45%, whereas the sign indicates that the ST values were lower than their SV counterparts.

In almost all presented cases the AP initiation site, where the target ANF starts the propagation of the nerve impulse, was the peripheral terminal of the fiber. The only exception was ANF680 where the AP is initiated in the ninth peripheral node, indicated by a square symbol in figure 7(a). Note that ANF680 has the highest electrode-node1 distance of 300 μm

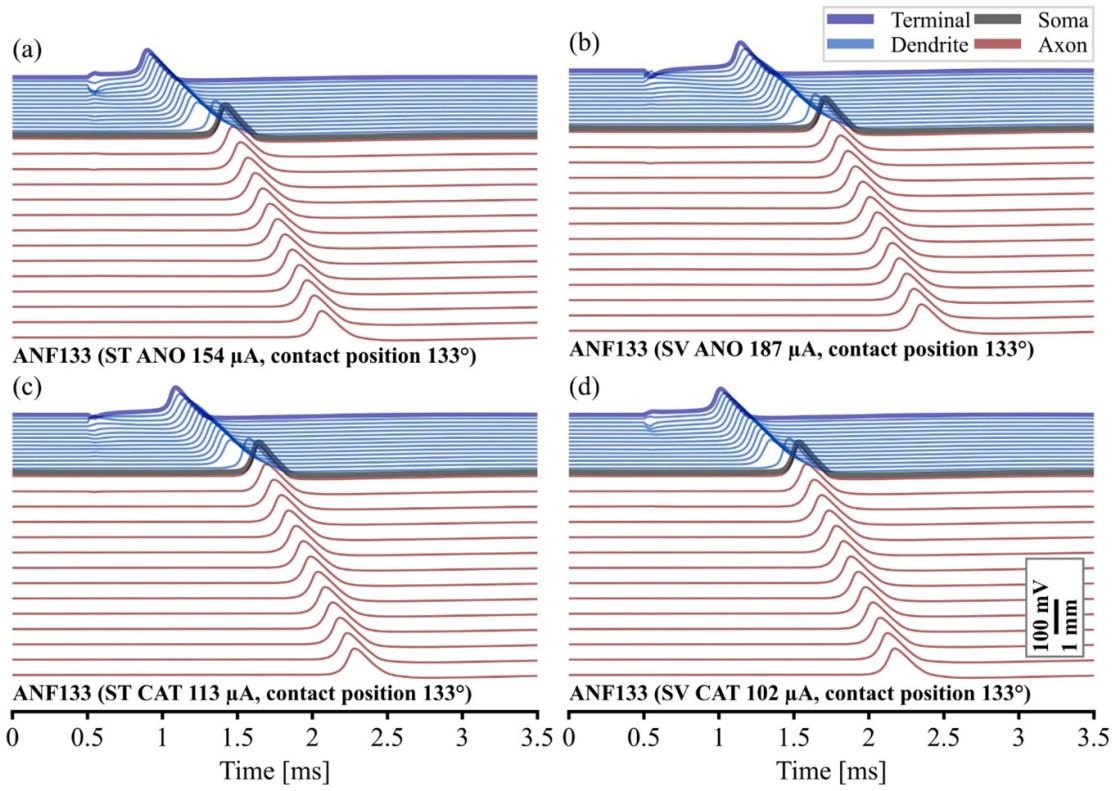

Figure 8. AP propagation in ANF133 for threshold stimulation. (a) ST ANO, (b) SV ANO, (c) ST CAT, (d) SV CAT. Each line indicates the temporal change in transmembrane voltage in selected compartments (terminal, dendritic nodes, soma, axon nodes). ST scala tympani, SV scala vestibuli, ANF auditory nerve fiber, ANO anodic, CAT cathodic.

(figure 6(c)) and is the most lateral electrode compared to its target ANF with a difference of −200 μm (figure 6(b)).

As an example, figure 8 shows the propagation of the induced AP in ANF133 for the ST electrode (left column), the SV electrode (right column) when CAT (bottom row) or ANO (top row) pulses are applied. Each line represents the temporal change in transmembrane potential ($V_m(t)$) in a specific compartment, i.e. the top curve shows $V_m(t)$ in the terminal followed by the $V_m(t)$ lines for the peripheral nodes, the soma, and the central nodes.

During CAT stimulation with the ST electrode (figure 8(c)) the terminal becomes hyperpolarized while the first three nodes get depolarized. The intracellular current flow allows for a transmembrane voltage distribution that is favorable for AP initiation in the terminal which happens 513 μs after stimulation onset. When CAT pulses are emitted from the SV electrode (figure 8(d)) the terminal gets depolarized directly initiating an AP slightly earlier after 438 μs. During ANO stimulation the opposite happens, i.e. during ST stimulation (figure 8(a)) there is a direct depolarization of the terminal which initiates the AP after 325 μs, while the terminal gets hyperpolarized for SV stimulation (figure 8(b)) but initiates the AP with a 575 μs delay. Consequently, thresholds are lower, and spikes are transmitted faster when the terminal gets directly depolarized.

3.4. Above-threshold stimulation

The stimulation amplitude not only determines the sensitivity but also the selectivity of the CI, i.e. how many fibers are stimulated in which sector of the cochlea. While the individual threshold stimulation specifically targets the closest fiber to a certain contact position, here we show the effects of CAT stimulation on all fibers for amplitudes of different strength (figure 9).

The lowest tested stimulus amplitude of 200 μA was already higher than the CAT threshold amplitudes of most of the fibers for ST and SV electrodes. But there were a few exceptions for the ST electrode in the range of 50–256° where the threshold of 6 fibers was above 200 μA, and for the SV electrode where ANF680 had a threshold of 318 μA (figure 7(a)). Thus, for some contact positions, not a single fiber initiated an AP at this stimulus amplitude indicated by the missing star symbol. Yet, there was already one case, the SV electrode at contact position 45°, where this low amplitude activated both its target ANF45 and its direct neighbor ANF50. Fibers in this sector of the cochlea showed a rather low CAT SV threshold of around ∼100–130 μA, i.e. the tested

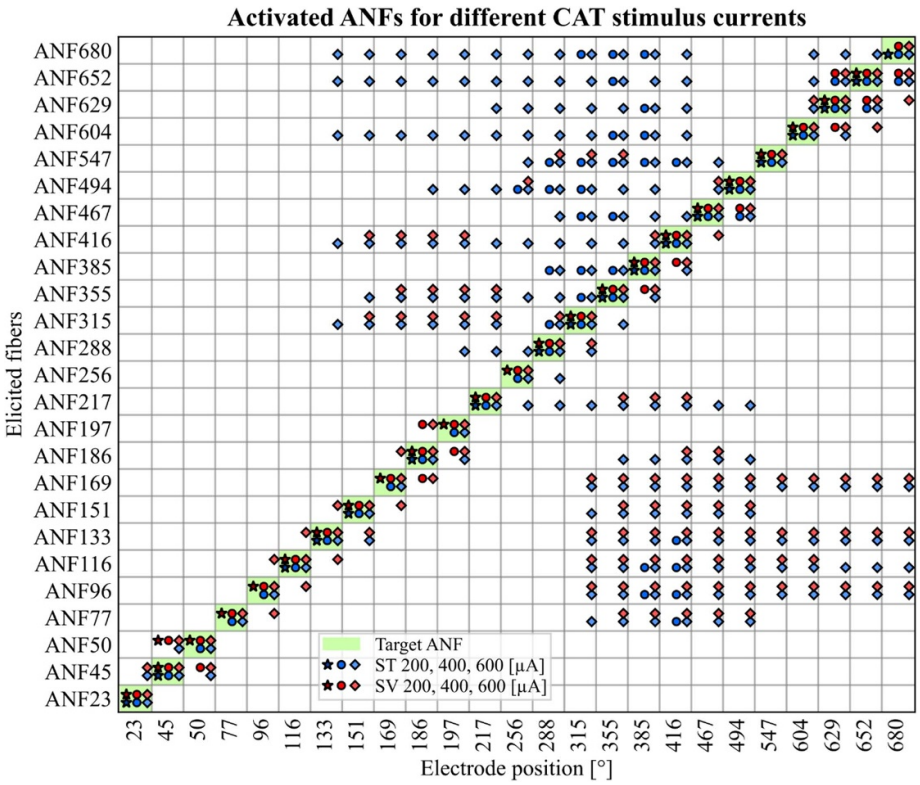

Figure 9. Spike elicitations for CAT stimulation for stimulation amplitudes of 200, 400, and 600 μA. The green diagonal marks the respective target fibers for each contact position. The lowest amplitude of 200 μA was already above the threshold of most of the fibers but not strong enough to trigger other fibers with the only exception at electrode contact position 45°. Raising the amplitude activates more fibers, and therefore to decreased selectivity. At the highest amplitude of 600 μA, focal stimulation was lost for electrode angles above 133°. ST scala tympani, SV scala vestibuli, ANF auditory nerve fiber, CAT cathodic.

amplitude of 200 μA is almost twice the minimum amplitude required to trigger APs in the respective target fibers. Furthermore, ANF45 and ANF50 are the closest neighboring fibers (section 3.1.) with a minimum angle difference of 5° between their terminals. Accordingly, the amplitude of 200 μA at contact position 45° already had quite a high impact on its neighbor. Interestingly, at SV electrode position 50° only the corresponding target fiber ANF50 triggered an AP, while ANF45 was not stimulated. A closer look at the exact pathways of these two fibers reveals that ANF50 starts at $\alpha = 50°$ and travels relatively straight to the cochlear axis, while ANF45 takes a slightly curved pathway in the counterclockwise direction towards the cochlear axis, away from its own target electrode and the electrode at 50°. Compare the top view of the second (ANF45) and third (ANF50) fibers in figure 2(b). Consequently, ANF45 has a bigger distance to the electrode of ANF50 than vice-versa and thus needs a higher stimulation current emitted by the SV electrode at 50° to initiate an AP.

Raising the stimulus amplitude current to 400 μA showed several additional fiber activations, especially for the ST electrodes between 256° and 416°. But also the SV electrode activated some direct neighbors of the respective target fibers. While the AP of activated direct neighbors was usually initiated in the terminal or peripheral dendritic nodes, most of the APs recorded in fibers farther away of the active contact were initiated in axonal nodes close to the soma. This is shown in detail in figure 10 for the ST electrode 385°, where the AP of the target fiber was initiated in the first two nodes of the peripheral dendrite, but the AP of the also activated ANF96 is initiated in the second axonal node close to the soma leading to a slightly faster arrival time of the AP at the end of the ANF.

For the highest amplitude of 600 μA, at almost every electrode position at least one direct neighbor of the target fiber was additionally activated. For electrode contact positions greater than 133° the selectivity of the CI decreased significantly, especially for the ST electrode which is more prone to activate more apical fibers while this is rarely seen for the SV electrode. However, for contact positions greater than 315° both electrodes show almost identical activation patterns of additional more basal fibers. Above this angle, the cochlea becomes much narrower, thus the active contacts are closer to the cochlear axis where they induce higher electric potentials along the axons of additional fibers that are spiraling down. With these high stimulation currents, the first section of the highly excitable axon (doubled dendritic diameter) triggers an AP through direct depolarization at a site which is a prominent candidate for spike initiation in various ANFs (figure 10). The exact activation pattern

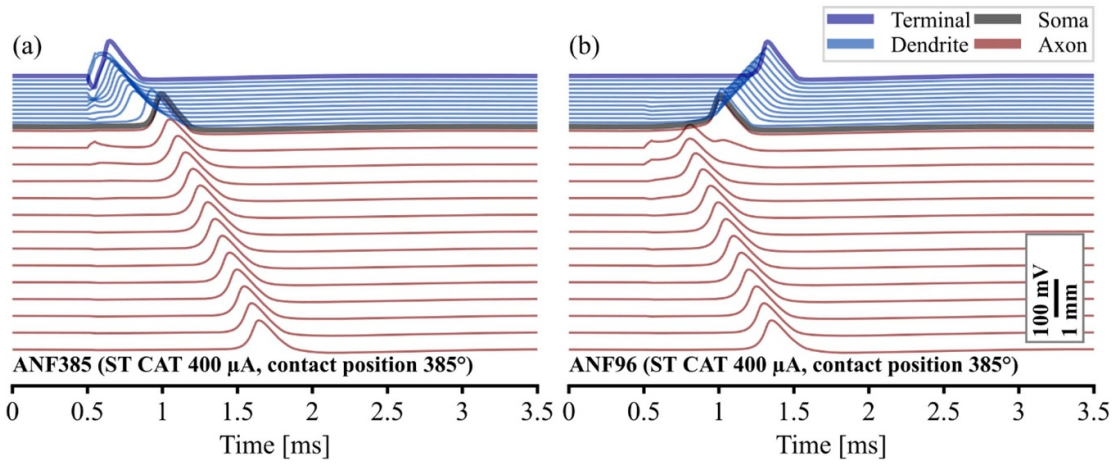

Figure 10. Above-threshold stimulation with 400 µA for contact position 385° activates target ANF385 (a) and co-stimulated ANF96 (b). While the target fiber AP is initiated in the first two dendritic nodes, the AP in ANF96 is initiated in the second axonal node due to the strong stimulus from the more apical electrode. AP action potential, ST scala tympani, ANF auditory nerve fiber, CAT cathodic.

of additional fibers not only depends on the stimulation strength, but also how close additional fibers are located to the active contact, and how the electric field from the contact is distributed inside the cochlea due to the varying electrical properties found in the different domains of the cochlea.

Raising the amplitude to even higher levels, ultimately leads to the activation of all fibers in the cochlea for both electrodes (not shown). Summarizing, in the CAT case, the SV array showed a much better selectivity at these levels of stimulation strength. As the fibers run top to bottom, the SV electrode contact is usually farther away from the highly active axon compared to the ST counterpart. These larger distances between an SV contact and the axons resulted in transmembrane potential levels that are too low to reach enough depolarization to induce an AP.

3.5. Variations in electrode angle

Since the threshold currents are sensitive to changes in the specific spatial relationship between electrode and target fiber, we additionally tested small shifts of the electrode contacts in both directions $\alpha = \{-9°, -6°, -3°, +3°, +6°, +9°\}$ for 5 selected fibers, ANF77, ANF193, ANF197, ANF288, ANF467 (figure 11). For each fiber ANO (positive) and CAT (negative) thresholds are presented for the ST electrode (blue symbols) and next to it for the SV electrode (red symbols). The threshold for the original electrode position ($\alpha = 0°$) is reproduced as a reference point (star symbols). Positive shifts are depicted as upward facing triangles, negative shifts with downward facing triangles, whereas the size of the symbol increases with the offset shift.

Shifting the electrode had varying effects on different target ANFs. The least affected fiber was ANF467, where especially for ST CAT and SV ANO the thresholds for the original and the shifted electrodes remained similar, i.e. the increase between maximum and minimum thresholds remained below 45%. The most affected target was ANF197, i.e. the highest increase of a three-fold maximum threshold compared to the minimum was recorded for ST CAT. Additionally, the biggest span in thresholds was seen for SV ANO. Corresponding values for electrode shifts of $\pm 9°$ were the two highest thresholds which are beyond the scale of the image.

However, the minimum threshold in a target ANF was not necessarily registered for the original electrode position with 0° offset. Specifically, the minimum threshold for ANO stimulation of ANF77 occurred for the ST electrode that was shifted by $-3°$. An electrode with a 3° offset was the most favorable for ANF197 and ST stimulation of both polarities, for ANF288 and SV stimulation of both polarities, and for ANF467 with SV CAT pulses. Additionally, in target ANF467 and ST stimulation of both polarities the minimum threshold was registered for electrodes with an offset of $-6°$.

For the selected target ANFs it may be concluded that the ANO thresholds are generally more sensitive to shifts of the SV electrode, whereas the CAT thresholds are often more affected by shifts of the ST electrode (broader spans of the recorded thresholds in figure 11). Although fibers were selected to be distributed along the cochlea, it cannot be ruled out that this behavior is specific to the presented ANFs. Moving the electrode in the clockwise (positive) or counterclockwise (negative) direction led to different changes in threshold amplitude. There was no clear pattern concerning either ST or SV electrode in terms of favorable offset direction. Yet, it can be said that for

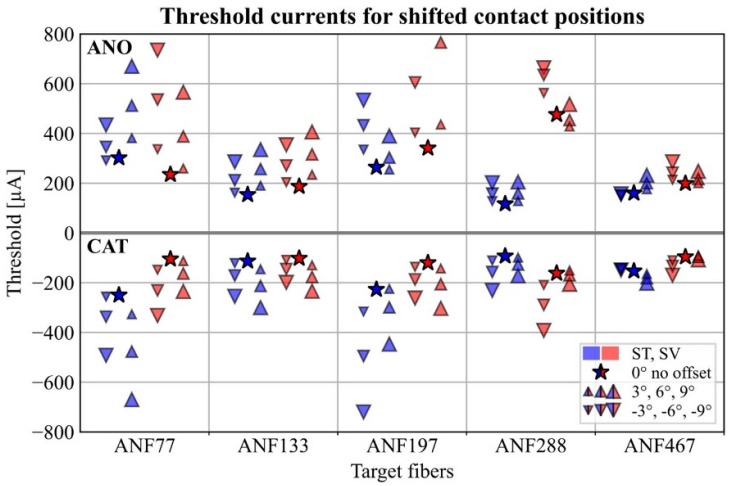

Figure 11. Positive ANO and negative CAT threshold currents for shifted electrode contact positions and selected target ANFs. ST thresholds are indicated in blue, SV thresholds in red. Star symbols mark the threshold for default contact position (0°, closest possible contact to the target ANF). Shifts are marked by triangles, whereas triangles pointing downward indicate negative angle shifts and triangle pointing upwards positive shifts. While there are fibers where a shifted active contact only results in minor threshold changes, other fibers show a higher sensitivity to the exact placement of the electrode contact. ST scala tympani, SV scala vestibuli, ANF auditory nerve fiber, ANO anodic, CAT cathodic.

both, ST and SV electrodes, the change in thresholds for varying offset remained similar when the pulse polarity is switched.

The APs were still initiated in the peripheral terminal, except for ANF197 with a −9°-shifted ST electrode and CAT stimulation where the spike started in the fifth peripheral node. It should further be noted, that in some cases additional ANFs were stimulated by the shifted target electrodes. Unsurprisingly, when the target electrode for ANF77 was shifted by +9° the neighboring ANF96 also got excited by the ST electrode irrespective of pulse polarity. This was also true for target ANF133, where ANF151 initiated an AP for SV CAT pulses and again both pulses of the ST electrode. The same electrode offset of +9° for target ANF197 also stimulated neighboring ANF217 by SV CAT pulses and even ANF315 by ST CAT pulses. For this target fiber, additionally, shifts in the negative direction starting from −6° also excited neighboring ANF186.

In summary, the results of this model predict a high sensitivity of thresholds on the specific ANF pathways considering changing curvature, bending of the processes, mid-modiolar spiraling patterns, as well as on the individual cochlear geometry and resulting possible electrode placements. The spatial relationship between target fiber and stimulating electrode crucially affected thresholds and AP initiation site.

4. Discussion

For typical neurons the axon is the most sensitive part during extracellular electrical stimulation (Nowak and Bullier 1998). Myelinated axons are easier to stimulate than non-myelinated fibers, threshold current is inversely related to fiber's diameter, and CAT fiber stimulation needs less current than ANO (Blair and Erlanger 1933, Ranck 1975). Threshold currents increase with the distance from the electrode (Ranck 1975) and hotspots for spike initiation are found where the gradient of the extracellular voltage is maximal (Eickenscheidt and Zeck 2014). These rules of thumb are confirmed by the analysis of compartment models (Rattay 1986, 1990, 1999, Rattay *et al* 2002).

4.1. Sodium channel bands in dendrites support spike initiation from lateral CI

Contrary to the common structure of a neuron, the dendrite of an afferent spiral ganglion neuron is myelinated and therefore this dendrite is often named 'peripheral axon'. The first short non-myelinated ANF segment between inner hair cell and habenula perforata is followed by a heminode which is longer than a node of Ranvier but also possesses a high concentration of sodium channels of Nav1.6 type. As this heminode is the spike generator during synaptic excitation from the hair cell it is also called axon initial segment (AIS) of the ANF (Kim and Rutherford 2016, Liu *et al* 2021). In the present study, the first ANF segment is called terminal and considered to be a single compartment of constant diameter (standard value 1.3 μm) with a length of 10 μm. This assumption has been adapted from previous studies (Colombo and Parkins 1987, Rattay 2000, Rattay *et al* 2001b) although the terminal might even be a bit longer and thinner before the ANF enters the habenula perforata. Yet, the previous modeling approach demonstrated that the terminal with its high density of sodium channels is still a hot spot for AP initiation, even

if other segments are exposed to larger stimulating forces. A homogenous 2D model with increased complexity of the lateral ANF micro-structure was used to verify that including a thin non-myelinated fiber segment between the inner hair cell and the 10 μm long terminal has no significant effect on threshold characteristics (data not shown).

Indeed, the presented results predict that for monophasic target stimulation of almost all ANFs the AP is initiated in the terminal despite its initial hyperpolarization for ST CAT and SV ANO pulses. We could show that current flow from a depolarized segment in the neighborhood quickly depolarizes the terminal where the high sodium channel density pushes the spike generation faster than in the primarily activated region (figures 8(b) and (c)). A similar observation has been reported previously (Potrusil *et al* 2020, Heshmat *et al* 2021, Rattay and Tanzer 2022) and the same shifting effect was also seen in retinal ganglion cells where spikes are generated in the sodium channel band even for electrode positions far away from this AIS (Werginz *et al* 2014).

4.2. Inverse stimulating forces for electrodes in SV and ST

The mechanisms behind AP initiation following extracellular stimulation are governed by the induced extracellular voltage profiles V_e along the ANF which in turn depend on the curvature of the electrode- fiber distance curves (Rattay 1999). During pulse application the extracellular voltage V_e oscillates along the ANF and a positive depolarization occurs in U-shaped regions of V_e; for more details see Potrusil *et al* (2020). For each ANF, the ST and SV active contacts have been placed at equivalent but opposite positions of the corresponding target fiber, which causes opposing stimulation effects in the vicinity of the electrode due to the mirrored behavior of the electrode-fiber distance curves. Indeed, we observed contrasting excitation patterns in the terminals of all 25 ANFs, i.e. if a pulse of a certain polarity from a ST electrode depolarizes the terminal, the same pulse from the SV electrode hyperpolarizes the terminal and vice versa. The same principle holds and is visible for the nodes close to the electrode. E.g. for ST ANO stimulation in figure 8 the sequence between positive (+) and negative (−) deviations from the resting membrane voltage for the terminal and node1 can be described as +,−. This sequence is mirrored to −,+ for a change in the scala (SV ANO) and also for a change in stimulus polarity (ST CAT), which caused similar excitation patterns in the diagonal subplots of figure 8.

However, irrespective of CI array placement either in ST or SV and regardless of pulse polarity, threshold amplitudes vary among different target ANFs. The specific threshold current depends on a variety of variables, e.g. its spatial relationship to the stimulating electrode and the inhomogeneous distribution of electric conductivity in the surrounding area which results in individual extracellular potential profiles along each ANF.

Our results allow for a comparison between the recorded threshold (figure 7(a)) and the difference in lateral distance of electrode contact to target ANF (figure 5(b)). In the ST case, if the electrode shifts to a more lateral position compared to its target ANF the thresholds tend to increase. Contrary, for SV electrodes the thresholds tend to decrease when the electrode moves to a more lateral position. In the CAT case, note that the maximum difference in lateral position of almost −200 μm for target ANF680 which has the highest recorded threshold.

Furthermore, results for the ST array predict decreasing thresholds for increasing the distance between the electrode contact and the ANF terminal (solid lines in figure 5(c)). This probably indicates that an increased bend of the peripheral terminal of the ANF results in a more pronounced peak in the V_e distribution along the ANF which leads to a lower threshold. This relationship is again reversed for the SV array, where increasing the electrode-terminal distance also increases the threshold amplitude. Again, note the clear outlier in CAT thresholds for ANF680 which has the highest distance of 300 μm.

In contrast, the correlation between the threshold currents and the electrode contact-node1 distance (dotted lines in figure 5(c)) indicates increasing ST and decreasing SV thresholds when then distance to the first node increases. In the ST case this probably means less curvature in the V_e distribution due to smaller variation in distances at the peripheral end of the dendrite (less pronounced bend). The reverse argument could be made in the SV case, i.e. with a closer first node the initial part might be bend towards the SV resulting in less variation of electrode-ANF distances at the start of the ANF.

Consequently, an increased variation in electrode-ANF distance curves at the start of the dendrite (figure 4(b)) is beneficial in both cases, the ST and SV CI array. This leads to more curvature and better-defined peaks in the V_e distributions and thus lower threshold currents. Indeed, a linear regression analysis predicts decreasing threshold for increasing difference in contact-terminal and contact-node1 distances for both arrays and both pulse polarities (data not shown).

Additionally, it should be noted that these electrode-ANF distances are crucially affected by the angle of the active contact along the electrode carrier (figure 5(a)). Already small shifts in the positive or negative direction of the active contact can impact the threshold amplitude of the target ANF (figure 11). Changes can be quite severe, and in some cases, thresholds might be even lower for a small shift of the target contact compared to the original position. However, these findings are of specific interest for the clinical situation, since active contacts of a CI array

close to a dead region might require high currents to elicit any relevant neural response. Although no clear pattern between offset direction and thresholds can be discerned for either ST or SV arrays, the predicted irregularities might also contribute to the variation found in threshold amplitudes of one group (ST ANO, ST CAT, SV ANO, SV CAT).

4.3. Suprathreshold stimulation

This study was restricted to a healthy neuronal status and lateral electrodes. Results predict generally higher ANO thresholds with only a few exceptions where the threshold is almost the same for both polarities (figure 7(c)). Therefore, only CAT suprathreshold stimulation was investigated for 200, 400 and 600 μA pulses to determine the limits of focal stimulation and the distribution of co-stimulated regions (figure 9). The CAT thresholds are mostly lower for SV electrodes compared to ST stimulation (figure 7(d)) and only a few target ANFs have CAT thresholds higher than the minimum tested amplitude of 200 μA (figure 7(a)). Figure 9 further indicates a difference in the pattern of co-stimulated ANFs between the two CI arrays, whereas in this case with lateral electrodes, the SV stimulation showed higher selectivity.

Focality is lost when problematic co-stimulation occurs in fibers that are from a different cochlear region and thus further away from the target ANF than its direct neighbors. This happens when the induced electric potential around the cochlear axis is raised above a critical value where it directly stimulates passing axons that are spiraling down (figure 10). For the ST array, first co-stimulation already occurs for a stimulation amplitude of 400 μA and electrode contacts above 256°. Even more critical is the situation for 600 μA, where ST contacts above 133° cause multiple AP elicitations in additional ANFs far away from their target. In comparison, co-stimulation for the SV array only occurs for 600 μA pulses from contacts above 151°. Furthermore, note that ANF256 has an ST threshold of 203 μA (figure 7(a)) which only needs to be doubled to cause spiking in ANF494, whereas the SV threshold of ANF256 is 121 μA which is just 20% of the critical 600 μA value needed for AP elicitation in the same ANF494.

It should be further emphasized that this situation might be different for an alternative peri-modiolar CI placement of the arrays. Potentially also changes in the angle of the electrode contact around the carrier (facing upwards in ST, and downwards in SV) could lead to a different outcome which might be investigated in the future.

4.4. Comparison with other modeling studies and clinical data

A big challenge of modeling studies is a realistic representation of ANF pathways including typical variations along the part of a human cochlea that is covered by CIs. Previous models simplified the 3D pathways by 1D animal models (Colombo and Parkins 1987) and human 2D models (Finley *et al* 1990, Rattay *et al* 2001a). The first human 3D model that considered the typical spiraled structure of spiral ganglion cells is based on an analytical geometrical approach (Kalkman *et al* 2014). Next steps were to include the fanning pattern seen in the lateral dendrites (compare figure 3 of Bai *et al* 2019) and traced data of human ANF bundles (Potrusil *et al* 2020). The directions of the lateral dendritic parts deviate from a regularly spiraled pattern as seen in the top view of figure 2 (e.g. the first five dendrites from ANF23 to ANF96). This is a result of non-systematically picking fibers during the tracing process which then included ANFs with several fanning patterns of their lateral dendrites.

The small number of 30 traced ANFs restricted a detailed analysis of the fanning effect. Yet, this selection is able to predict more details in threshold variations compared to regularly curved ANFs that were studied before the findings of Bai *et al* (2019). This fanning effect is expected to contribute to the oscillating irregularities in threshold amplitudes for one CI array and one pulse polarity as seen in figure 7(a). Furthermore, for lateral electrodes the fan-like dendritic endings enlarge the dynamic range, which is the stimulus intensity interval causing a 10%–90% spiking probability in a target ANF (Miller *et al* 1999). Although the distance between dendrite and electrode is the main contributing factor in a regular model, the fan angle additionally affects the dynamic range. Furthermore, the impact of ion current fluctuations on the dynamic range is larger for dendrites than for axon stimulation (Rattay and Tanzer 2022). Thus, both, the ion current fluctuations and the fanning effect help to explain why more sound intensity levels can be discriminated by lateral electrodes (Kreft *et al* 2004, Wardrop *et al* 2005).

In addition to the previously mentioned clinical results comparing the quality in speech understanding for ST and SV implants, a recent study (SV, $n = 12$; ST, $n = 21$) confirmed that auditory outcomes are similar in both groups after one year after cochlear implantation: Speech recognition of words was 49 $\pm$ 7.6% and 56 $\pm$ 5.0% in quiet and 75 $\pm$ 9.5% and 66 $\pm$ 6.0% in noise in SV and ST groups, respectively (Gu *et al* 2023). In summary, the reported equal speech quality in silence and noise and most of the other reports agree with threshold similarities of ST and SV electrodes observed in our modeling study. Yet, it should be noted that these observed similarities might be a direct result of the specific alignment of electrode carriers in ST and SV and equivalent placement of active contacts. Different outcomes in terms of comparability might be observed when the CIs are moved individually to more lateral positions within the respective cochlear duct or when they are shifted towards the cochlear axis. Furthermore, it is plausible that the relationship between ST and SV stimulation

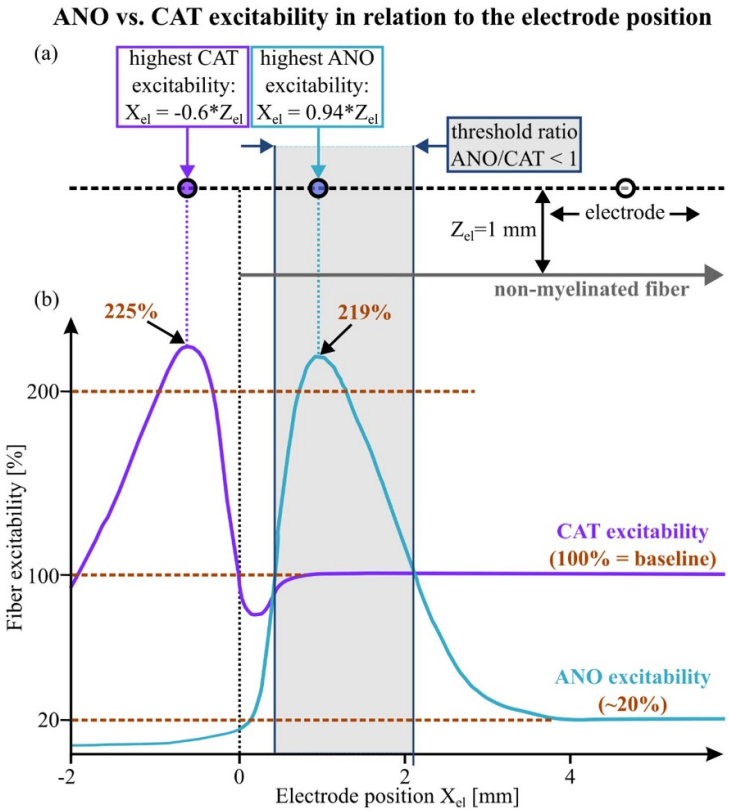

Figure 12. ANO versus CAT excitability of a straight fiber depends on electrode positions X_{el} along the axon. (a) The electrode is moved in 1 mm distance (Z_{el}) above the fiber. Most efficient electrode placements are marked for CAT and ANO stimulation as violet and turquoise filled circles respectively. The only area where the fiber is more sensitive to ANO currents, i.e. ANO/CAT < 1, is indicated in grey and corresponds to X_{el} values of about double the electrode—fiber distance Z_{el}. (b) Fiber excitability is defined as the maximum voltage along the fiber at the end of a constant subthreshold stimulus, whereas each point of the curve represents this maximum for a given electrode position X_{el}. Excitability curves are normalized with reference to the CAT 'central' excitation where the fiber ending has no impact anymore. Thus, this constant value for CAT stimulation (violet curve) represents the baseline of 100% excitability. The ANO excitability curve reaches its constant value of about 20% for electrodes that are placed at a distance of about 4 times the electrode-fiber distance Z_{el} from the start of the fiber. The characteristic shape of the excitability curves holds within a certain range of Z_{el} and therefore the position for the highest excitability is also expressed relative to the electrode—fiber distance. Model aspects: non-myelinated fiber with Hodgkin Huxley dynamics; monopolar point source stimulation, homogeneous medium; for more model details see Rattay (2008). ANO anodic, CAT cathodic.

might be additionally altered if different degeneration levels of the ANFs are considered (Heshmat *et al* 2020, Wenger *et al* 2023a, 2023b).

While some clinical studies of ST implants report similar thresholds for CAT and ANO stimulation (Macherey *et al* 2006) essentially lower thresholds for ANO currents were observed (Macherey *et al* 2008, Undurraga *et al* 2010). This controversy may be based on the fact that the ANO/CAT threshold ratio depends on the electrode position, the dynamic range and the neural status (Macherey *et al* 2008). The intense impact of electrode placements close to the terminal region was previously demonstrated for an electrode that is moved at a constant distance of 1 mm along a straight non-myelinated nerve fiber (Rattay 2008). The main findings are reproduced in figure 12 which shows fiber excitability as a function of changing electrode position X_{el} for ANO (turquoise curve) and CAT stimulation (violet curve). Fiber excitability is defined as the maximum voltage of the fiber at the end of a subthreshold pulse. For larger X_{el} (about 1 and 4 mm for CAT and ANO pulses, respectively) the impact of the terminal is completely lost resulting in constant excitability curves. For such a central electrode site the fiber is essentially more sensitive to CAT stimulation corresponding to a threshold ratio of 0.2 which is in the range of reported values for both myelinated and non-myelinated nerve fibers and also independent of the fiber diameter (Ranck 1975, Rattay 1990). Moving the electrode from a central place towards the peripheral terminal, the CAT excitability is reduced before it again reaches 100% at $X_{el} = 0$ and a peak value of 225% at $X_{el} = -0.6$ mm. The range of excitability is remarkably larger for ANO stimulation (peak value: 219%) with quite low values if the electrode is preceding the terminal, i.e. in front of or before the start of the fiber. This straight fiber example demonstrates that the impact of the terminal is one key element for large variations in the threshold ratio while others are mentioned in sections 4.1–4.3. In addition, the threshold ratio depends on the soma size and the number of cell membranes covering the soma, i.e. poor soma myelination with only 1–3 sheets plus dendritic loss are indicators for a low

threshold ratio (Potrusil *et al* 2020). The dependency of the threshold ratio on the degree of degeneration has been investigated for typical types of pulses emitted by lateral and peri-modiolar electrodes (Heshmat *et al* 2021) and has also already been discussed for SV electrodes in a homogenous 2D model (Wenger *et al* 2023b).

4.5. Limitations of the study and future directions

The main objective of this study was to present a first approach to investigate the excitability of ANFs in response to CI implantation into the SV, and to compare it to results obtained from ST stimulation. The intention is to start bridging the gap between the numerous presented clinical reports and the lack of related modeling studies. We hope to foster future discussion about alternative SV CI placement specifically in the case of highly obstructed ST.

However, this initial computational study was based on a single human dataset including a small set of traced ANFs and only one pair of equivalent CI arrays in ST and SV at a lateral position. Due to the high sensitivity on electrode-fiber spatial relationships, more scanned ANF pathways would be beneficial to study the spread of excitation. A systematic study could be conducted on how specific curvature changes of the ANF pathway influence the spiking pattern. Additionally, the choice of parameters in the compartment model that is imposed on the ANFs affects the electric behavior of a stimulated fiber. The length of the dendritic internodes determines the position of the peripheral nodes of Ranvier, where the electrical potential is evaluated to compute the ion currents. To compensate for the neglected stochastic distribution of these active areas, we reduced the length of the dendritic internodes since the original value of 250 μm was rather high. Although the general excitation pattern of ANFs remained the same, using a dendritic internodal length of 125 μm slightly reduced threshold variations among fibers. Another possible and related refinement might be to include the stochasticity of spiking as consequence of ion current fluctuations (Rattay and Tanzer 2022). For a comparison between different compartment models and their compatibility with experimental observations see Bachmaier *et al* (2019). Importantly, following studies should analyze the impact of neuronal degeneration on the ANF's excitability, i.e. ongoing degeneration is usually modelled by decreasing the diameter of the dendrite and reducing the number of myelin sheets around peripheral internodes, whereas complete degeneration often considers the total loss of the dendrite.

Ongoing investigations will further concentrate on varying CI placement. Currently we focused on aligned electrode arrays within ST and SV, although a more lateral placement of the silicone carrier would have been possible in both cases and peri-modiolar CIs could also be analyzed. Furthermore, active contacts have been placed at equivalent positions on the ST and SV electrode to directly target an individual ANF. Different distributions of stimulating contacts along and around the electrode carriers shall be tested in the future.

Additional to the spatial relation of electrode and target ANF, the V_e distributions depend on the electrical properties, specifically the electrical conductivity in the different domains of the model. It should be noted that while the electric current induced by ST stimulation needs to cross the modiolus domain, the current from the SV electrode can travel within liquids of high conductivity. In this model we distinguish the three cochlear ducts, the surrounding bone and the modiolus only, whereas other studies additionally consider own domains with a specific conductivity for the Basilar and Reissner's membrane, the organ of Corti, and the spiral ligament (Kalkman *et al* 2015, Nogueira *et al* 2016). Also it is possible that the resistance of the Reissner membrane may have an impact on the threshold amplitudes, especially for SV electrodes. The conductance of the organ of Corti could be included in the future for more accurate results concerning the excitation of the terminal. Furthermore, some electric conductivity values differ among modeling studies, specifically for the modiolus which has a rather low conductivity in the current study. The modiolus is assumed to be a homogenous domain, although it represents a complex aggregate of nerve tissue and bony structures. Thus, it is difficult to define an optimal scalar conductivity, which should be investigated in more detail during a sensitivity analysis of electrical properties. Moreover, it will be crucial to clarify how ossification alters induced thresholds for ANF stimulation in a ST with decreasing conductivity. To simulate different degrees and sites of ossification, future studies might also introduce an inhomogeneous conductivity distribution within the ST to reveal further detail on the impact of the ANFs excitability.

5. Conclusion

With this study we show that CI arrays in ST and SV with equivalent active contacts relative to target fibers can elicit similar neural response which confirms that SV implantation may be an alternative for patients with a highly obstructed ST. For aligned and equivalent electrodes, the SV array showed a much better selectivity at these levels of stimulation strength. As the fibers run top to bottom, the SV electrode contact is usually farther away from the highly active axon compared to the ST counterpart. This study further emphasizes the need for realistic fiber pathways when studying extracellular stimulation since anatomically correct irregularities that are present throughout the cochlea impact threshold amplitudes and general recruitment sensitivity. Consequently,

the hearing performance following CI stimulation of every patient will be crucially affected by the specific degeneration pattern and remaining pathways of intact fibers, as well as individual cochlear geometry and resulting options for surgical implantation.

Data availability statement

The data that support the findings of this study are available upon reasonable request from the authors.

Acknowledgments

This work was supported by the Austrian Science Fund (FWF), Grant No. P36271-N. Further, the authors acknowledge TU Wien Bibliothek for financial support through its Open Access Funding Program.

ORCID iDs

Andreas Fellner https://orcid.org/0000-0003-3704-8764
Cornelia Wenger https://orcid.org/0000-0001-7889-9093
Amirreza Heshmat https://orcid.org/0000-0002-2052-152X
Frank Rattay https://orcid.org/0000-0002-2819-8827

References

Arbuthnott E R, Boyd I A and Kalu K U 1980 Ultrastructural dimensions of myelinated peripheral nerve fibres in the cat and their relation to conduction velocity *J. Physiol.* **308** 125–57
Arnesen A R and Osen K K 1978 The cochlear nerve in the cat: topography, cochleotopy, and fiber spectrum *J. Compar. Neurol.* **178** 661–78
Bacciu S, Bacciu A, Pasanisi E, Vincenti V, Guida M, Barbot A and Berghenti T 2002 Nucleus multichannel cochlear implantation in partially ossified cochleas using the Steenerson procedure *Otol. Neurotol.* **23** 341–5
Bachmaier R, Encke J, Obando-Leitón M, Hemmert W and Bai S 2019 Comparison of multi-compartment cable models of human auditory nerve fibers *Front. Neurosci.* **13** 1173
Bai S, Encke J, Obando-Leitón M, Weiß R, Schäfer F, Eberharter J, Böhnke F and Hemmert W 2019 Electrical stimulation in the human cochlea: a computational study based on high-resolution micro-CT scans *Front. Neurosci.* **13** 1312
Balkany T, Gantz B J, Steenerson R L and Cohen N L 1996 Systematic approach to electrode insertion in the ossified cochlea *Otolaryngol. Head Neck Surg.* **114** 4–11
Blair E A and Erlanger J 1933 A comparison of the characteristics of axons through their individual electrical responses *Am. J. Physiol.-Legacy Content* **106** 524–64
Carnevale N T and Hines M L 2006 *The NEURON Book* (Cambridge University Press) (https://doi.org/10.1017/CBO9780511541612)
Cignoni P, Callieri M, Corsini M, Dellepiane M, Ganovelli F and Ranzuglia G 2008 MeshLab: an open-source mesh processing tool *6th Eurographics Italian Chapter Conf.* pp 129–36
Coelho D H and Roland J T 2012 Implanting obstructed and malformed cochleae *Otolaryngol. Clin. North Am.* **45** 91–110
Colombo J and Parkins C W 1987 A model of electrical excitation of the mammalian auditory-nerve neuron *Hear. Res.* **31** 287–311
Dhanasingh A and Jolly C 2017 An overview of cochlear implant electrode array designs *Hear. Res.* **356** 93–103
Eickenscheidt M and Zeck G 2014 Action potentials in retinal ganglion cells are initiated at the site of maximal curvature of the extracellular potential *J. Neural Eng.* **11** 036006
Fellner A, Heshmat A, Werginz P and Rattay F 2022 A finite element method framework to model extracellular neural stimulation *J. Neural Eng.* **19** 022001
Finley C C, Holden T A, Holden L K, Whiting B R, Chole R A, Neely G J and Skinner M W 2008 Role of electrode placement as a contributor to variability in cochlear implant outcomes *Otol. Neurotol.* **29** 920–8
Finley C C, Wilson B S and White M W 1990 Models of neural responsiveness to electrical stimulation *Cochlear Implants: Models of the Electrically Stimulated Ear* ed J M Miller and F A Spelman (Springer) pp 55–96
Geier L L and Norton S J 1992 The effects of limiting the number of nucleus 22 cochlear implant electrodes programmed on speech perception *Ear Hear.* **13** 340–8
Green J D Jr, Marion M S and Hinojosa R 1991 Labyrinthitis ossificans: histopathologic consideration for cochlear implantation *Otolaryngol. Head Neck Surg.* **104** 320–6
Gu W, Daoudi H, Lahlou G, Sterkers O, Ferrary E, Nguyen Y, Mosnier I and Torres R 2023 Auditory outcomes after scala vestibuli array insertion are similar to those after scala tympani insertion 1 year after cochlear implantation *Eur. Archiv. Oto-Rhino-Laryngol.* **281** 155–62
Hanekom T and Hanekom J J 2016 Three-dimensional models of cochlear implants: a review of their development and how they could support management and maintenance of cochlear implant performance *Network* **27** 67–106
Heshmat A, Sajedi S, Johnson Chacko L, Fischer N, Schrott-Fischer A and Rattay F 2020 Dendritic degeneration of human auditory nerve fibers and its impact on the spiking pattern under regular conditions and during cochlear implant stimulation *Front. Neurosci.* **14** 599868
Heshmat A, Sajedi S, Schrott-Fischer A and Rattay F 2021 Polarity sensitivity of human auditory nerve fibers based on pulse shape, cochlear implant stimulation strategy and array *Front. Neurosci.* **15** 751599
Hlden L K *et al* 2013 Factors affecting open-set word recognition in adults with cochlear implants *Ear Hear.* **34** 342–60
Hochmair I, Hochmair E, Nopp P, Waller M and Jolly C 2015 Deep electrode insertion and sound coding in cochlear implants *Hear. Res.* **322** 14–23
Hodgkin A L and Huxley A F 1952 A quantitative description of ion currents and its applications to conduction and excitation in nerve *J. Physiol.* **117** 500–44
Holzmeister C, Andrianakis A, Kiss P, Moser U and Graupp M 2022 Scala vestibuli cochlear implant supported by 3D modeling of the inner ear *Wien. Klin. Wochenschr.* **134** 5–6
Hossain W A, Antic S D, Yang Y, Rasband M N and Morest D K 2005 Where is the spike generator of the cochlear nerve? Voltage-gated sodium channels in the mouse cochlea *J. Neurosci.* **25** 6857–68
Kalkman R K, Briaire J J, Dekker D M T and Frijns J H M 2014 Place pitch versus electrode location in a realistic computational model of the implanted human cochlea *Hear. Res.* **315** 10–24
Kalkman R K, Briaire J J and Frijns J H M 2015 Current focussing in cochlear implants: an analysis of neural recruitment in a computational model *Hear. Res.* **322** 89–98
Kerr J and Backous D D 2005 Cochlear implantation in the partially ossified cochlea *Operative Tech. Otolaryngol.-Head Neck Surg.* **16** 113–6
Kiefer J, Weber A, Pfennigdorff T and Von Ilberg C 2000 Scala vestibuli insertion in cochlear implantation: a valuable alternative for cases with obstructed scala tympani *ORL* **62** 251–6

Kim K X and Rutherford M A 2016 Maturation of nav and kv channel topographies in the auditory nerve spike initiator before and after developmental onset of hearing function *J. Neurosci.* **36** 2111–8

Kreft H A, Donaldson G S and Nelson D A 2004 Effects of pulse rate and electrode array design on intensity discrimination in cochlear implant users *J. Acoust. Soc. Am.* **116** 2258–68

Lee S, Mendel L L and Bidelman G M 2019 Predicting speech recognition using the speech intelligibility index and other variables for cochlear implant users *J. Speech Lang. Hear. Res.* **62** 1517–31

Leonor A and Santiago Luis A 2004 Bilateral cochlear implant user with a right ear scala vestibuli insertion and left ear scala tympani insertion: case report *Int. Congr. Ser.* **1273** 455–8

Liu W, Luque M, Li H, Schrott-Fischer A, Glueckert R, Tylstedt S, Rajan G, Ladak H, Agrawal S and Rask-Andersen H 2021 Spike generators and cell signaling in the human auditory nerve: an ultrastructural, super-resolution, and gene hybridization study *Front. Cell. Neurosci.* **15** 642211

Macherey O, Carlyon R P, Van Wieringen A, Deeks J M and Wouters J 2008 Higher sensitivity of human auditory nerve fibers to positive electrical currents *J. Assoc. Res. Otolaryngol.* **9** 241–51

Macherey O, Van Wieringen A, Carlyon R P, Deeks J M and Wouters J 2006 Asymmetric pulses in cochlear implants: effects of pulse shape, polarity, and rate *J. Assoc. Res. Otolaryngol.* **7** 253–66

Miller C A, Abbas P J, Robinson B K, Rubinstein J T and Matsuoka A J 1999 Electrically evoked single-fiber action potentials from cat: responses to monopolar, monophasic stimulation *Hear. Res.* **130** 197–218

Motz H and Rattay F 1986 A study of the application of the Hodgkin-Huxley and the Frankenhaeuser-Huxley model for electrostimulation of the acoustic nerve *Neuroscience* **18** 699–712

Nadol J B 1988 Comparative anatomy of the cochlea and auditory nerve in mammals *Hear. Res.* **34** 253–66

Nogueira W, Schurzig D, Büchner A, Penninger R T and Würfel W 2016 Validation of a cochlear implant patient-specific model of the voltage distribution in a clinical setting *Front. Bioeng. Biotechnol.* **4** 84

Nowak L G and Bullier J 1998 Axons, but not cell bodies, are activated by electrical stimulation in cortical gray matter. I. Evidence from chronaxie measurements *Exp. Brain Res.* **118** 477–88

O'Connell B P, Hunter J B, Haynes D S, Holder J T, Dedmon M M, Noble J H, Dawant B M and Wanna G B 2017 Insertion depth impacts speech perception and hearing preservation for lateral wall electrodes *Laryngoscope* **127** 2352–7

O'Connell B P, Hunter J B and Wanna G B 2016 The importance of electrode location in cochlear implantation *Laryngoscope Invest. Otolaryngol.* **1** 169–74

Pijl S and Noel F 1992 The nucleus multichannel cochlear implant: comparison of scala tympani vs. scala vestibuli electrode placement in a single patient *Otolaryngol. Head Neck Surg.* **107** 472–4

Potrusil T, Heshmat A, Sajedi S, Wenger C, Chacko L J, Glueckert R, Schrott-Fischer A and Rattay F 2020 Finite element analysis and three-dimensional reconstruction of tonotopically aligned human auditory fiber pathways: a computational environment for modeling electrical stimulation by a cochlear implant based on micro-CT *Hear. Res.* **393** 108001

Potrusil T, Wenger C, Glueckert R, Schrott-Fischer A and Rattay F 2012 Morphometric classification and spatial organization of spiral ganglion neurons in the human cochlea: consequences for single fiber response to electrical stimulation *Neuroscience* **214** 120–35

Ranck J B 1975 Which elements are excited in electrical stimulation of mammalian central nervous system: a review *Brain Res.* **98** 417–40

Rattay F 1986 Analysis of models for external stimulation of axons *IEEE Trans. Biomed. Eng.* **BME-33** 974–7

Rattay F 1990 *Electrical Nerve Stimulation* (Springer) (https://doi.org/10.1007/978-3-7091-3271-5)

Rattay F 1999 The basic mechanism for the electrical stimulation of the nervous system *Neuroscience* **89** 335–46

Rattay F 2000 Basics of hearing theory and noise in cochlear implants *Chaos Solitons Fractals* **11** 1875–84

Rattay F 2008 Current distance relations for fiber stimulation with pointsources *IEEE Trans. Biomed. Eng.* **55** 1122–7

Rattay F and Aberham M 1993 Modeling axon membranes for functional electrical stimulation *IEEE Trans. Biomed. Eng.* **40** 1201–9

Rattay F, Greenberg R J and Resatz S 2002 Neuron modeling *Handbook of Neuroprosthetic Methods* (CRC Press) (https://doi.org/10.1201/9781420040876.ch3)

Rattay F, Leao R N and Felix H 2001a A model of the electrically excited human cochlear neuron. II. Influence of the three-dimensional cochlear structure on neural excitability *Hear. Res.* **153** 64–79

Rattay F, Lutter P and Felix H 2001b A model of the electrically excited human cochlear neuron. I. Contribution of neural substructures to the generation and propagation of spikes *Hear. Res.* **153** 43–63

Rattay F, Potrusil T, Wenger C, Wise A K, Glueckert R and Schrott-Fischer A 2013 Impact of morphometry, myelinization and synaptic current strength on spike conduction in human and cat spiral ganglion neurons *PLoS One* **8** e79256

Rattay F and Tanzer T 2022 Impact of electrode position on the dynamic range of a human auditory nerve fiber *J. Neural Eng.* **19** 016025

Rinia A B, Olphen A F and Dunnebier E A 2006 Cochlear implantation in obstructed cochleas: the effect of the degree of obstruction on the number of activated electrodes and the amount of postoperative speech perception *Clin. Otolaryngol.* **31** 280–6

Schnabl J, Glueckert R, Feuchtner G, Recheis W, Potrusil T, Kuhn V, Wolf-Magele A, Riechelmann H and Sprinzl G M 2012 Sheep as a large animal model for middle and inner ear implantable hearing devices: a feasibility study in cadavers *Otol. Neurotol.* **33** 481–9

Shaul C, Dragovic A S, Stringer A K, O'Leary S J and Briggs R J 2018 Scalar localisation of peri-modiolar electrodes and speech perception outcomes *J. Laryngol. Otol.* **132** 1000–6

Spoendlin H and Schrott A 1989 Analysis of the human auditory nerve *Hear. Res.* **43** 25–38

Steenerson R L, Gary L B and Wynens M S 1990 Scala vestibuli cochlear implantation for labyrinthine ossification *Otol. Neurotol.* **11** 360–3 (available at: https://journals.lww.com/otology-neurotology/abstract/1990/09000/SCALA_VESTIBULI_COCHLEAR_IMPLANTATION_FOR.14.aspx)

Tang Q, Benítez R and Zeng F G 2011 Spatial channel interactions in cochlear implants *J. Neural Eng.* **8** 046029

Trudel M, Côté M, Philippon D, Simonyan D, Villemure-Poliquin N and Bussières R 2018 Comparative impacts of scala vestibuli versus scala tympani cochlear implantation on auditory performances and programming parameters in partially ossified cochleae *Otol. Neurotol.* **39** 700–6

Undurraga J A, Van Wieringen A, Carlyon R P, Macherey O and Wouters J 2010 Polarity effects on neural responses of the electrically stimulated auditory nerve at different cochlear sites *Hear. Res.* **269** 146–61

Wardrop P, Whinney D, Rebscher S J, Luxford W and Leake P 2005 A temporal bone study of insertion trauma and intracochlear position of cochlear implant electrodes. II:

comparison of Spiral Clarion™ and HiFocus II™ electrodes *Hear. Res.* **203** 68–79

Wenger C, Fellner A, Bucek F, Werginz P and Rattay F 2023a Simulating auditory nerve fiber response following micro-electrode stimulation *Curr. Directions Biomed. Eng.* **9** 5–8

Wenger C, Fellner A, Bucek F, Werginz P and Rattay F 2023b Comparison of cochlear implant electrode placement in the scala tympani vs scala vestibuli: simulating auditory nerve fiber response of varying degeneration degree *Bernstein Conf.* (https://doi.org/10.12751/nncn.bc2023.262)

Werginz P, Fried S I and Rattay F 2014 Influence of the sodium channel band on retinal ganglion cell excitation during electric stimulation—a modeling study *Neuroscience* **266** 162–77

World Report on Hearing 2021 Geneva: World Health Organization Licence: CC BY-NC-SA 3.0 IGO

Yukawa K, Cohen L, Blamey P, Pyman B, Tungvachirakul V and O'Leary S 2004 Effects of insertion depth of cochlear implant electrodes upon speech perception *Audiol. Neurotol.* **9** 163–72

Zeitler D M, Lalwani A K, Roland J T, Habib M G, Gudis D and Waltzman S B 2009 The effects of cochlear implant electrode deactivation on speech perception and in predicting device failure *Otol. Neurotol.* **30** 7–13

Zeng F-G 2022 Celebrating the one millionth cochlear implant *JASA Express Lett.* **2** 077201

Zeng F-G, Rebscher S, Harrison W, Sun X and Feng H 2008 Cochlear implants: system design, integration, and evaluation *IEEE Rev. Biomed. Eng.* **1** 115–42